Available online at www.sciencedirect.com
ScienceDirect
Journal of Computational Physics 227 (2008) 4354–4397
JOURNAL OF COMPUTATIONAL PHYSICS
www.elsevier.com/locate/jcp

A local directional ghost cell approach for incompressible viscous flow problems with irregular boundaries

Petter A. Berthelsen *, Odd M. Faltinsen

Centre for Ships and Ocean Structures, Norwegian University of Science and Technology, Otto Nielsens veg. 10, NO-7491 Trondheim, Norway

Received 8 October 2007; accepted 28 December 2007
Available online 9 January 2008

Abstract

An immersed boundary method for the incompressible Navier–Stokes equations in irregular domains is developed using a local ghost cell approach. This method extends the solution smoothly across the boundary in the same direction as the discretization it will be used for. The ghost cell value is determined locally for each irregular grid cell, making it possible to treat both sharp corners and thin plates accurately. The time stepping is done explicitly using a second order Runge–Kutta method. The spatial derivatives are approximated by finite difference methods on a staggered, Cartesian grid with local grid refinements near the immersed boundary. The WENO scheme is used to treat the convective terms, while all other terms are discretized with central schemes. It is demonstrated that the spatial accuracy of the present numerical method is second order. Further, the method is tested and validated for a number of problems including uniform flow past a circular cylinder, impulsively started flow past a circular cylinder and a flat plate, and planar oscillatory flow past a circular cylinder and objects with sharp corners, such as a facing square and a chamfered plate.

MSC: 65M06; 65M50; 76D05; 76M20

PACS: 02.60.Cb; 02.70.Bf; 47.11.Bc

Keywords: Incompressible Navier–Stokes equation; Immersed boundary method; Ghost cell method; Cartesian grid; Irregular domain; Finite difference methods

1. Introduction

Flow problems involving complex geometries still poses a difficult challenge in computational fluid dynamics. Traditional methods use body-fitted grids, structured or unstructured, that conforms to the solid

* Corresponding author. Current address: MARINTEK, P.o. Box 4125 Valentinlyst, NO7450 Trondheim, Norway. Tel.: +47 73510034; fax: +47 73595967.
E-mail addresses: P.A.Berthelsen@marintek.sintef.no (P.A. Berthelsen), oddfal@marin.ntnu.no (O.M. Faltinsen).
URLs: http://www.cesos.ntnu.no/~petterab (P.A. Berthelsen), http://www.marin.ntnu.no/~oddfal (O.M. Faltinsen).

0021-9991/$ - see front matter © 2008 Elsevier Inc. All rights reserved.
doi:10.1016/j.jcp.2007.12.022

boundary. However, the difficulty of generating high-quality grids increases with the complexity of the geometry and much effort must be put into the pre-processing stage. An alternative approach is to use so-called immersed boundary methods, sometimes referred to as Cartesian grid methods, where the boundary intersects with an underlying Cartesian grid. No complexity is involved in generating the Cartesian grid and most standard numerical schemes can be used, although some modifications to the discretization are required in the vicinity of the immersed boundary.

Several different immersed boundary methods can be found in the literature. They can be classified as either diffuse (continuous) methods or sharp (discrete) methods [49,51]. The diffuse methods are considered to be somewhat simpler to use than the sharp category, but it is not straightforward how the boundary conditions should be imposed at the immersed boundary. The immersed boundary method as proposed by Peskin [55,56] was originally developed to handle elastic boundaries for simulating blood flow in the heart, but has later been used to simulate flow with rigid boundaries, e.g. [38,63]. The boundary conditions are enforced through a smoothed forcing term added to the momentum equation. Other examples of diffuse methods can be found in [22,61,86,53], among others.

One disadvantage with diffuse methods is that the effect of the boundary is distributed over a band of several grid points which smear out discontinuities across the boundary. This smearing has an unfavorable effect on the accuracy of the numerical scheme. More accurate schemes can be found among the category of sharp methods. In these methods the numerical discretization near the immersed boundary is modified so that the boundary conditions are imposed directly at the location of the boundary. The cut-cell method is such an approach used within the finite volume framework [13,57,73,83,85]. Grid cells cut by the immersed boundary are reshaped to conform to the boundary. This reshaping may in some cases result in very small grid cells with an adversely impact on the numerical stability. To overcome this problem, cell-merging strategies have been successfully proposed [57,85]. However, due to the many possible configurations of the irregular cut-cell, particularly in three dimensions, implementation becomes a tedious and non-trivial task.

Fadlun et al. [14] proposed to reconstruct the solution at grid nodes in the flow field nearest to the immersed boundary using some form of interpolation, or external forcing, to enforce the sharp boundary conditions. This approach does not affect the numerical stability since the numerical operators can remain unchanged; however, the crucial issue is more related to how the solution is reconstructed near the boundary [21]. Fadlun et al. [14] used a one-dimensional interpolation along the grid line intersecting the solid boundary, but the choice of interpolation direction may seem to be arbitrary in the case of more geometrically complex shaped boundaries. Later, Balaras [1] introduced a reconstruction scheme where the solution is reconstructed along a well-defined line normal to the body. Similar ideas can be found in [20,21,82]. These methods do not solve any equation at the first grid point external to the boundary [14]. It should be stressed that Fadlun et al. [14] enforced the boundary condition on the tentative velocity field, which does not satisfy the divergence constraint, before correcting the velocity due to the updated pressure field. They argue that the correction obtained from the projection step introduced only small errors in the treatment of the immersed boundaries.

For finite difference methods, the numerical operators near the immersed boundary can be explicitly modified to include points at the boundary instead of grid points inside the solid region [74,46,49,84]. Marella et al. [49] obtained valid finite difference expressions for the first- and second-derivatives using Taylor series expansions involving only grid points on one side of the boundary. This approach is somewhat analogous to the cut-cell method for finite volume schemes, but only one single configuration of a numerical operator is needed since modifications to the discretization stencil depends only on the distance to the boundary and not the shape of the irregular cell. The numerical stability of the modified stencil may be altered if the boundary is very close to a grid point. One way of avoiding this problem is to move the boundary slightly within a grid cell [49], which locally decreases the order of accuracy.

An other sharp interface approach is the immersed interface method (IIM). The IIM as proposed by Leveque and Li [41] was developed to solve elliptic problems with discontinuous and non-smooth solutions. Standard finite difference methods work poorly for these problems since the Taylor expansions are not valid for non-smooth functions. In the IIM, correction terms are added to the numerical discretization to account for any jump in the solution or its derivative. The original IIM has been modified for various sharp interface problems (e.g. [4,32,42,43,47,77]), and it has also been extended to solve incompressible flow problems with

solid boundaries [9,44,45,81,39]. It should be noted that every type of discretization stencils have their own unique correction term.

The use of ghost cells introduce an alternative way of imposing the boundary conditions. Traditional ghost cell methods assume that analytical continuation of the solution across the boundary is possible. Ghost cells are fictitious cells inside the solid which are updated by extrapolating values from the flow field and the boundary. The numerical operators do not need to be reformulated near the boundary, instead the boundary conditions are implicitly incorporated through the ghost cells. There are numerous ways of extrapolating values into the ghost cells. A local flow variable is commonly represented in terms of a polynomial which is used to evaluate the ghost point. The accuracy of the ghost cell depends on the order of the interpolation scheme used to obtain this polynomial [70]. Higher order polynomials are more accurate but also known to be more sensitive to numerical instabilities.

Majumdar et al. [48] and Tseng and Ferziger [70,71] use two-dimensional linear and quadratic interpolation involving fluid nodes in the vicinity of the boundary and boundary points to construct the local polynomial. To remedy potential instabilities they introduce an image point I inside the fluid along the normal to the boundary which goes through the ghost node G (see Fig. 1). The concept of using an image point in the wall-normal direction has been widely used by others (e.g. [6,7,18,75]). Obtaining a wall-normal direction, however, is not always straightforward, instead Tremblay and Friedrich [68] use a weighted combination of one-dimensional extrapolations to update their ghost cells. Their weighting coefficients depend only on the distance to the wall, where the direction closest to the boundary is given the largest weighting.

While a wall-normal or multi-directional approach of obtaining the ghost cell value may seem like a natural choice for smooth boundaries it is not that obvious for more irregular shaped geometries. For instance, if the geometry consist of a sharp corner, as in Fig. 2(a), extending the solution across the immersed boundary in the y-direction $(B - G)$ does not necessarily create a solution which is continuous across the boundary in the x-direction $(A - G)$, and *vice versa*. Analytical continuation is not possible since the interior solution is not single valued. For this reason, the direction of the extrapolation does also influence the accuracy of the method. Another problem associated with ghost cell methods is encountered, as shown in Fig. 2(b), if a thin plate, e.g. a trailing edge, separates two active grid nodes. For this problem, the ghost cells must lie inside the fluid domain requiring separate memory locations [17]. The sharp interface methods of Udayakumar et al. [74] and Marella et al. [49] are well suited for such irregular shapes, but unlike their approaches the ghost cell method utilizes a simple extension to more advanced schemes since no changes need to be applied to the numerical discretization. The external forcing approach of e.g. [14] can also handle such complex geometries, but discretization stencils involving grid cells beyond the neighbouring node would then require a wide band of inactive grid cells inside the fluid domain which are updated by interpolation.

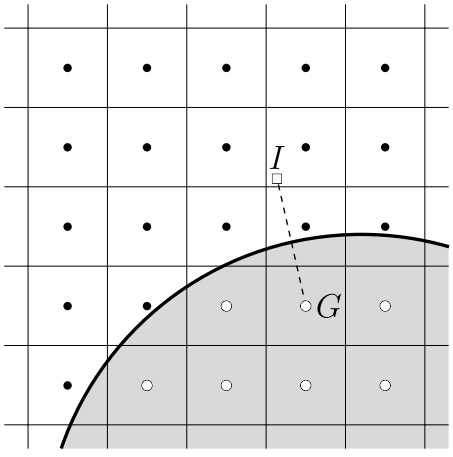

Fig. 1. Illustration of a ghost cell (G) using an image point (I).

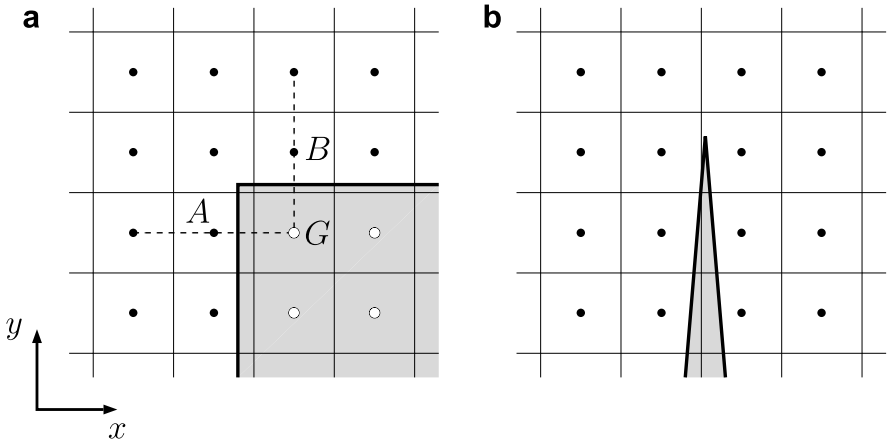

Fig. 2. Irregular shaped geometries: (a) a sharp corner and (b) a thin plate.

In this work, we present an immersed boundary method capable of solving the incompressible Navier–Stokes equations in the presence of highly irregular boundaries. The main idea is to use a local directional ghost cell which is obtained by one-dimensional extrapolation along the same direction as the discretization it will be used for. As for the example in Fig. 2(a), the ghost cell needs to be determined twice, along the x- and y-directions, respectively. Each irregular grid cell has its own set of local ghost cells because of the topological differences. Similar concepts have been used when solving elliptic equations on irregular domains (e.g. [19,87]). The present approach differs from other ghost cell methods mainly in the way the ghost cell values are extrapolated and updated. The ghost cells are updated such that the velocity field satisfies both the immersed boundary condition and the incompressibility constraint at the end of each time step. We also present a method to avoid numerical instabilities associated with grid nodes located close to the boundary without reducing the formal accuracy. Also, a block structured grid refinement procedure is adopted to efficiently resolve large variations in the flow near the immersed boundary.

The rest of the paper is organized as follows: In Section 2 the basic idea behind the ghost cell method is outlined using a one-dimensional approach. The governing equations are presented in Section 3. Then, in Section 4, the numerical method for solving the incompressible Navier–Stokes equations is described in detail, including the treatment of the immersed boundary and the local grid refinement strategy. Numerical results are presented in Section 5 before we summarize with a conclusion in Section 6.

2. A one-dimensional ghost cell approach

Traditional finite difference methods cannot be applied to discontinuous and non-smooth functions since the Taylor expansion is not valid for such problems. But, if the function is piecewise smooth it is possible to devise a technique that conforms to any jump in the function and its higher derivatives. For simplicity, consider a generic, one-dimensional function $f(x), x \in [x_{\min}, x_{\max}]$, which is analytic everywhere except at the interior point $x = x_\alpha (x_{\min} < x_\alpha < x_{\max})$,

$$f(x) = \begin{cases} f^-(x) & \text{if } x_{\min} \leqslant x \leqslant x_\alpha, \\ f^+(x) & \text{if } x_\alpha < x \leqslant x_{\max}. \end{cases}$$

The computational domain $[x_{\min}, x_{\max}]$ can be discretized into $N+1$ grid points with uniform grid spacing $\Delta x = (x_{\max} - x_{\min})/N$. The grid coordinates are defined as $x_i = x_{\min} + i\Delta x$ for $0 \leqslant i \leqslant N$ and f_i denotes $f(x_i)$. Then, for any continuous and smooth region $x_l < x_i < x_r$ we can write the numerical approximation to the nth-derivative of $f(x_i)$ as

$$f_i^{(n)} = \mathcal{L}^{(n)}(f_l, f_{l+1}, \ldots, f_i, \ldots, f_{r-1}, f_r) + \mathcal{O}(\Delta x^p), \tag{1}$$

where $L^{(n)}$ denotes the discrete finite difference operator and p is the order of accuracy of the numerical approximation. The width of the discretization stencil, $r - l + 1$, depends on the given finite difference scheme.

Next, let the interface be located at $x_\alpha = x_j + a\Delta x$ where $0 \leqslant a < 1$ and $i \leqslant j < r$ such that the grid cells x_j and x_{j+1} are separated by the interface. The finite difference approximation (1) can no longer be applied since that involves grid cells on both sides of the interior point x_α. However, since $f(x)$ is piecewise analytic it can be smoothly extended beyond the interface by means of a fictitious domain (see Fig. 3). As a result, the standard finite difference operator $\mathcal{L}^{(n)}$ can be applied to approximate the nth-derivative of $f(x_i)$,

$$f_i^{(n)} = \mathcal{L}^{(n)}(f_l, f_{l+1}, \ldots, f_i, \ldots, f_j, f_{j+1}^g, \ldots, f_{r-1}^g, f_r^g) + \mathcal{O}(\Delta x^{\bar{p}}), \tag{2}$$

where the function values $f_{j+1}, \ldots, f_r$ are replaced by fictitious ghost cell values $f_{j+1}^g, \ldots, f_r^g$.

The ghost cell values can be determined by, for instance, fitting a qth order Lagrange polynomial, $p_q(x)$, to the points $x_{j-q+1}, \ldots, x_j$ and x_α, where

$$p_q(x) = \left(\sum_{s=j-q+1}^{j} \beta_s(x) f_s \right) + \beta_\alpha(x) f_\alpha^- \tag{3}$$

for

$$\beta_s(x) = \left(\prod_{\substack{t=j-q+1 \\ t \neq s}}^{j} \frac{x - x_t}{x_s - x_t} \right) \frac{x - x_\alpha}{x_s - x_\alpha}, \qquad \beta_\alpha(x) = \prod_{t=j-q+1}^{j} \frac{x - x_t}{x_\alpha - x_t}$$

and

$$f_\alpha^- = \lim_{x \to x_\alpha^-} f(x).$$

The polynomial $p_q(x)$ approximates $f(x)$ to the left of x_α, and it gives a smooth extension of $f^-(x)$ at $x_{j+1}, \ldots, x_r$ with the truncation error $\mathcal{O}(\Delta x^{q+1})$. The error introduced by the ghost cells in the numerical approximation of $f_i^{(n)}$ will then be of $\mathcal{O}(\Delta x^{q+1-n})$ since the nth-derivative operator $\mathcal{L}^{(n)}$ involves a division by Δx^n. The order of accuracy of the finite difference discretization (2) is therefore $\bar{p} = \min(p, q+1-n)$; hence, the local accuracy of the numerical scheme is preserved if $q \geqslant p + n - 1$.

The polynomial approximation (3) may present some difficulties if the interior point x_α is very close to x_j. This is due to the singular behaviour of β_j and β_α as $|x_j - x_\alpha| \to 0$. To avoid this unfavorable behaviour we introduce an image point defined as

$$x_\gamma = x_j - \max(0, \epsilon - a)\Delta x = x_\alpha - \max(a, \epsilon)\Delta x,$$

where ϵ is a predefined positive constant chosen such that if $a \geqslant \epsilon$ then Eq. (3) exhibits no singular behaviour. Further, we reconstruct $f(x_\gamma)$ using a qth order Lagrange polynomial and the grid points $x_{j-q}, \ldots, x_j$, i.e.

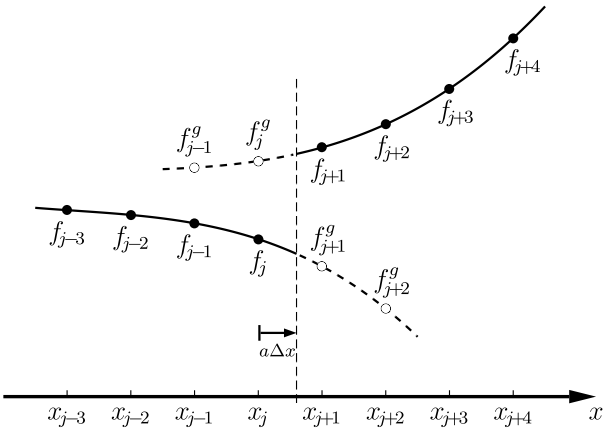

Fig. 3. Illustration of a smoothly extended discontinuous function $f(x)$. Actual function values (●); fictitious ghost cell values (○).

$$f_\gamma = p_q(x_\gamma) = \sum_{s=j-q}^{j} \left(\prod_{\substack{t=j-q \\ t\neq s}}^{j} \frac{x_\gamma - x_t}{x_s - x_t} \right) f_s.$$

The ghost cells can then be updated by the qth order polynomial fitted to the points $x_{j-q+1}, \ldots, x_\gamma$ and x_α,

$$p_q(x) = \left(\sum_{s=j-q+1}^{j-1} \beta_s(x) f_s \right) + \beta_\alpha(x) f_\alpha^- + \beta_\gamma(x) f_\gamma, \tag{4}$$

where

$$\beta_s(x) = \left(\prod_{\substack{t=j-q+1 \\ t\neq s}}^{j-1} \frac{x - x_t}{x_s - x_t} \right) \frac{(x - x_\alpha)(x - x_\gamma)}{(x_s - x_\alpha)(x_s - x_\gamma)}, \qquad \beta_\alpha(x) = \left(\prod_{t=j-q+1}^{j-1} \frac{x - x_t}{x_\alpha - x_t} \right) \frac{x - x_\gamma}{x_\alpha - x_\gamma}$$

and

$$\beta_\gamma(x) = \left(\prod_{t=j-q+1}^{j-1} \frac{x - x_t}{x_\gamma - x_t} \right) \frac{x - x_\alpha}{x_\gamma - x_\alpha}.$$

This way, none of the denominators in the β-coefficients become smaller than ϵ as long as $\epsilon \leqslant 0.5$, and the formal accuracy of the ghost cells are preserved. Effectively, this is the same as using a weighted combination of the extrapolations involving the grid points $x_{j-q+1}, \ldots, x_j, x_\alpha$ and $x_{j-q}, \ldots, x_{j-1}, x_\alpha$.

3. Governing equations

Consider a two-dimensional Cartesian computational domain Ω containing an immersed solid boundary in the form of a simple closed curve, Γ, dividing Ω into two separate sub-domains Ω^+ and Ω^-. Here Ω^+ denotes the fluid region and Ω^- denotes the solid body. The fluid is assumed to be an incompressible, Newtonian fluid described by the non-dimensional Navier–Stokes equations without the effect of gravity

$$\nabla \cdot \mathbf{u} = 0, \qquad \mathbf{x} \in \Omega^+, \tag{5}$$

$$\frac{\partial \mathbf{u}}{\partial t} + \mathbf{u} \cdot \nabla \mathbf{u} = -\nabla p + \frac{1}{Re} \nabla^2 \mathbf{u}, \qquad \mathbf{x} \in \Omega^+, \tag{6}$$

where $\mathbf{u} = (u, v)$ is the fluid velocity normalized with respect to a characteristic velocity scale U, $\mathbf{x} = (x, y)$ denotes the Cartesian coordinates normalized by a characteristic length scale D, t is the time normalized by D/U, and p is the pressure normalized by ρU^2 where ρ is the mass density of the fluid. The Reynolds number is defined as $Re = UD/\nu$ where ν is the kinematic viscosity.

Further, boundary conditions for the velocity and the pressure field must be prescribed at the immersed boundary. Requiring no slip at the solid boundary for a fixed, non-moving body yields

$$\mathbf{u} = \mathbf{u}_\Gamma \equiv \mathbf{0}, \quad \mathbf{x} \in \Gamma. \tag{7}$$

For the pressure field, boundary conditions can be obtained from the momentum Eq. (6) in each axis direction as

$$\frac{\partial p}{\partial x} = \frac{1}{Re} \nabla^2 u \quad \text{and} \quad \frac{\partial p}{\partial y} = \frac{1}{Re} \nabla^2 v, \quad \mathbf{x} \in \Gamma, \tag{8}$$

since the left hand side of Eq. (7) vanishes at the boundary. Projecting these conditions onto the unit normal $\mathbf{n}$ to the solid boundary Γ gives the following Neumann boundary condition:

$$\mathbf{n} \cdot \nabla p = \frac{\partial p}{\partial n} = \mathbf{n} \cdot \frac{1}{Re} \nabla^2 \mathbf{u}, \quad \mathbf{x} \in \Gamma.$$

Boundary conditions at the exterior boundary $\partial\Omega$ and initial conditions must also be applied in order to close the system.

4. Numerical method

In this section, the numerical method for solving incompressible flow in complex geometries is presented. This scheme is based on the well-known projection method [10] where an intermediate velocity field is first obtained from an approximation of the momentum Eq. (6), then an elliptic equation is solved for the pressure which enforces the divergence constraint (5).

In this work the time stepping is done explicitly using a second order predictor–corrector method. The spatial derivatives are approximated by finite difference discretization on a staggered grid. A fifth order WENO scheme [30,31] is used to treat the convective terms in Eq. (6) while central schemes are used for all other terms. A local grid refinement technique is used to efficiently resolve the boundary layer flow near the immersed boundary. The details of the numerical scheme are outlined below.

4.1. Time-stepping procedure

The following predictor–corrector procedure is a Runge–Kutta method based on the trapezoidal rule, also known as Heun's method. The two steps of the projection method are done twice at each time step to ensure that only a divergence-free velocity field is used in the different terms of Eq. (6). At the predictor stage, an Euler step is taken to advance the solution with the time step Δt. Let

$$\mathcal{F}(\mathbf{u}) = -\mathbf{u}\cdot\nabla\mathbf{u} + \frac{1}{Re}\nabla^2\mathbf{u}, \tag{9}$$

then, using a time-discrete form,

$$\mathbf{u}^* = \mathbf{u}^n + \Delta t\mathcal{F}(\mathbf{u}^n)$$

and

$$\bar{\mathbf{u}}^{n+1} = \mathbf{u}^* - \Delta t\nabla\bar{p},$$

where $\bar{p}$ is obtained from solving

$$\nabla^2\bar{p} = \frac{1}{\Delta t}\nabla\cdot\mathbf{u}^*. \tag{10}$$

The predicted velocities, $\bar{\mathbf{u}}^{n+1}$, are then used in the corrector step to obtain the solution at time t^{n+1},

$$\mathbf{u}^{**} = \mathbf{u}^n + \frac{\Delta t}{2}\left(\mathcal{F}(\mathbf{u}^n) + \mathcal{F}(\bar{\mathbf{u}}^{n+1})\right) \tag{11}$$

and

$$\mathbf{u}^{n+1} = \mathbf{u}^{**} - \Delta t\nabla\hat{p}, \tag{12}$$

where $\hat{p}$ is calculated from

$$\nabla^2\hat{p} = \frac{1}{\Delta t}\nabla\cdot\mathbf{u}^{**}. \tag{13}$$

Appropriate numerical boundary conditions for the Poisson equation (13) can be obtained by rearranging Eq. (12),

$$\nabla\hat{p} = \frac{\left(\mathbf{u}_\Gamma^{**} - \mathbf{u}_\Gamma^{n+1}\right)}{\Delta t} \quad \text{at } \mathbf{x}\in\Gamma. \tag{14}$$

By setting $\mathbf{u}_\Gamma^{**} = \mathbf{u}_\Gamma^{n+1}$ the boundary conditions (8) are implicitly satisfied, leading to a simpler homogeneous boundary condition for the pressure when solving Eq. (13),

$$\nabla\hat{p} = 0 \quad \text{at } \mathbf{x}\in\Gamma.$$

Similar arguments can be used to obtain the numerical boundary condition at the exterior boundary if the velocity is prescribed at time t^{n+1} (e.g. walls and inlets). If the exterior boundary is an outlet it is common to apply a Dirichlet boundary condition for the pressure,

$$\hat{p} = p_{\text{outlet}} \quad \text{at } \mathbf{x} \in \partial\Omega_{\text{outlet}}.$$

The boundary conditions for $\bar{p}$ when solving Eq. (10) are the same as given for $\hat{p}$ above where $\mathbf{u}^{**}$ is replaced by $\mathbf{u}^{*}$.

It follows from Eqs. (11) and (12) that if we define

$$p^{n+1/2} = \hat{p}$$

then not only the velocity field is second order accurate in time but also the pressure. Thus, the pressure field is lagged in time. Second order temporal accuracy for the pressure at t^{n+1} is obtained by extrapolation, i.e.

$$p^{n+1} = p^{n+1/2} + \frac{\Delta t}{2}\frac{\partial p^{n+1/2}}{\partial t} \approx p^{n+1/2} + \frac{\Delta t}{2}\left(\frac{p^{n+1/2} - p^{n-1/2}}{t^{n+1/2} - t^{n-1/2}}\right).$$

4.2. Spatial discretization

The governing equations are discretized using a staggered grid: the velocity components are defined at the appropriate cell faces, $u_{i+1/2,j}$ and $v_{i,j+1/2}$, and the pressure is defined at the cell centres, $p_{i,j}$. Here, the subscript i,j indicates the grid cell (i,j) in index space or $\mathbf{x}_{i,j} = (x_i, y_j)$ in physical space, the subscript $i+1/2, j$ indicates the cell face separating cell (i,j) and $(i+1,j)$ at $\mathbf{x}_{i+1/2,j}$, and $i, j+1/2$ indicates the cell face separating cell (i,j) and $(i,j+1)$ at $\mathbf{x}_{i,j+1/2}$. The uniform grid cell spacing for each grid level are denoted Δx and Δy in x- and y-direction, respectively. Where it is appropriate, we have dropped the superscript n for the ease of notation in the remaining sections.

4.2.1. Relationship between the grid and the immersed boundary

Before we proceed with the details of the spatial discretizations a relationship between the grid and the immersed boundary needs to be established. In order to have a practical representation of the immersed boundary, the body surface is discretized into a number of piecewise linear elements. There are no restrictions on the size of these elements so that any curved surface can be represented to desired accuracy by simply using a sufficiently large number of elements. A simpler representation of the immersed boundary is possible using the zero level set of a distance function; however, the level set formulation fails to describe sharp corners and infinitely thin plates.

Grid cells where the cell centre is inside the solid are defined as inactive, while the cells where the cell centre is outside the solid are defined as active. An active grid cell is said to be irregular if at least one neighbouring grid cell is separated by an immersed boundary; otherwise, it is defined as regular. A velocity point is active if and only if grid cells on both sides of that cell face are active and there are no immersed boundary separating the two cell centre points (see Fig. 4).

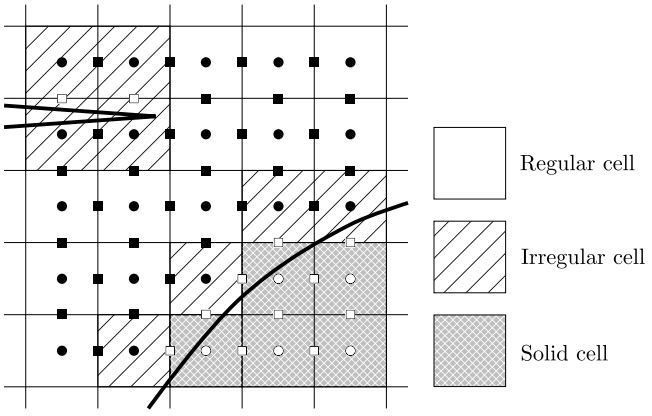

Fig. 4. Definition of active and inactive grid points. Active pressure point (●); inactive pressure point (○); active velocity point (■); inactive velocity point (□).

Some inactive velocity points may still lie in the fluid. These velocity points are referred to as boundary points. It should be noted that these boundary points are marked as inactive only because no pressure gradients can be obtained at these points due to the lack of active pressure cells on both sides of the point. In order to have a well-defined problem, the velocity components defined as boundary points are updated by interpolation using the no-slip condition at the immersed boundary and active velocity points within the fluid. This procedure may seem similar to e.g. [14], but we would like to emphasize that there are still active velocity points adjacent to the boundary. Here, we have used a one-dimensional, third order interpolation scheme. For instance, as shown in Fig. 5(a), let $\mathbf{x}_{i+1/2,j}$ be the location of the boundary point and $u_{i+1/2,j}$ be the interpolated velocity, then the one-dimensional interpolation in x-direction is given as (skipping the j-index)

$$u_{i+1/2} = \sum_{s=i-2}^{i} \left(\prod_{\substack{t=i-2 \\ t\neq s}}^{i} \frac{x_{i+1/2} - x_{t-1/2}}{x_{s-1/2} - x_{t-1/2}} \right) \frac{x_{i+1/2} - x_\Gamma}{x_{s-1/2} - x_\Gamma} u_{s-1/2} + \left(\prod_{t=i-2}^{i} \frac{x_{i+1/2} - x_{t-1/2}}{x_\Gamma - x_{t-1/2}} \right) u_\Gamma,$$

where u_Γ is the wall boundary condition located at x_Γ, and $u_{i-1/2}, u_{i-3/2}$ and $u_{i-5/2}$ are values taken from the neighbouring points $x_{i-1/2}, x_{i-3/2}$ and $x_{i-5/2}$, respectively.

If a boundary point can be interpolated from more than one direction, each direction is weighted by a multiplication factor [67,68], i.e.

$$u_{i+1/2,j} = \gamma_x u^x_{i+1/2,j} + \gamma_y u^y_{i+1/2,j}, \tag{15}$$

where the weighting coefficients are given as

$$\gamma_x = \frac{1}{1 + \left(\frac{a\Delta x}{b\Delta y}\right)^2} \quad \text{and} \quad \gamma_y = \frac{1}{1 + \left(\frac{b\Delta y}{a\Delta x}\right)^2}$$

and the distance between the immersed surface and the boundary point in x and y-directions are $a\Delta x$ and $b\Delta y$, respectively (see Fig. 5(b)). This way the nearest surface element will give the largest influence on the velocity component.

4.2.2. Discretization of the momentum equation

For now, let us assume that all velocity nodes involved in the discretizations below are active and located far away from any boundary surface so that the finite difference stencils are all well-defined and valid.

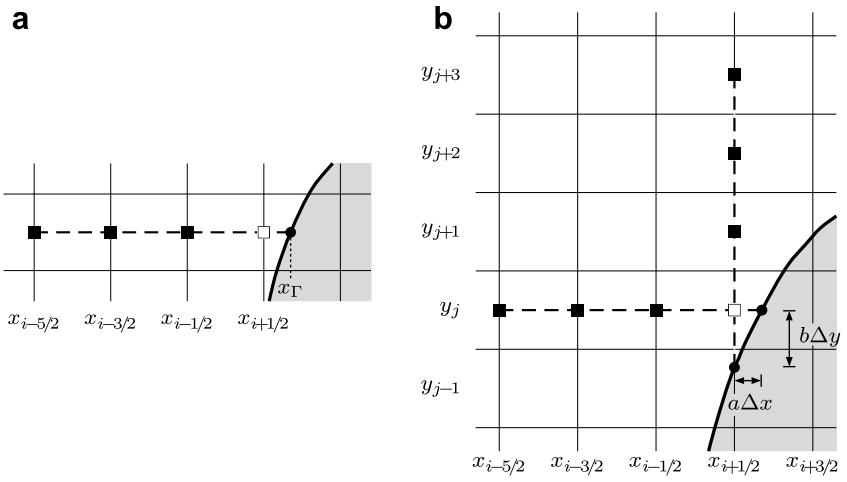

Fig. 5. Reconstruction of boundary points: (a) One-dimensional interpolation in x-direction. (b) Multi-directional interpolation. Inactive boundary point (□); active velocity points (■); wall points on immersed boundary (●).

We define a set of cell centre velocities with simple averaging:

$$u_{i,j} = \frac{u_{i-1/2,j} + u_{i+1/2,j}}{2} \quad \text{and} \quad v_{i,j} = \frac{v_{i,j-1/2} + v_{i,j+1/2}}{2}. \tag{16}$$

In order to update u and v on the appropriate cell faces, we also need to define u at the cell face $(i, j+1/2)$ and v at $(i+1/2, j)$. Simple averaging gives

$$u_{i,j+1/2} = \frac{u_{i,j} + u_{i,j+1}}{2} \quad \text{and} \quad v_{i+1/2,j} = \frac{v_{i,j} + v_{i+1,j}}{2}. \tag{17}$$

Let us now consider the x-component of the momentum equation. The second-derivatives in the viscous term are dicretized using standard second order accurate central differencing at the cell faces. We get

$$(\nabla^2 u)_{i+1/2,j} = (u_{xx})_{i+1/2,j} + (u_{yy})_{i+1/2,j},$$

where

$$(u_{xx})_{i+1/2,j} = \frac{u_{i+3/2,j} - 2u_{i+1/2,j} + u_{i-1/2,j}}{\Delta x^2}$$

and

$$(u_{yy})_{i+1/2,j} = \frac{u_{i+1/2,j+1} - 2u_{i+1/2,j} + u_{i+1/2,j-1}}{\Delta y^2}.$$

The convective terms, uu_x and vu_y, are discretized using a fifth order upwind WENO scheme [30,31]. For the first-derivative in the x-direction, $(u_x)_{i+1/2,j}$, the upwind procedure gives us

$$(u_x)_{i+1/2,j} = \begin{cases} u_x^- & \text{if } u_{i+1/2,j} > 0, \\ u_x^+ & \text{if } u_{i+1/2,j} < 0, \\ 0 & \text{otherwise,} \end{cases}$$

where the WENO approximation is a convex combination of the three possible ENO3 approximations,

$$u_x^\pm = \omega_1^\pm u_x^{1\pm} + \omega_2^\pm u_x^{2\pm} + \omega_3^\pm u_x^{3\pm}.$$

The three ENO3 stencils are defined as

$$u_x^{1\pm} = \frac{q_1^\pm}{3} - \frac{7q_2^\pm}{6} + \frac{11q_3^\pm}{6},$$
$$u_x^{2\pm} = -\frac{q_2^\pm}{6} + \frac{5q_3^\pm}{6} + \frac{q_4^\pm}{3},$$
$$u_x^{3\pm} = \frac{q_3^\pm}{3} + \frac{5q_4^\pm}{6} - \frac{q_5^\pm}{6},$$

where

$$q_1^- = \frac{u_{i-3/2,j} - u_{i-5/2,j}}{\Delta x}, \quad q_2^- = \frac{u_{i-1/2,j} - u_{i-3/2,j}}{\Delta x}, \quad q_3^- = \frac{u_{i+1/2,j} - u_{i-1/2,j}}{\Delta x}, \quad q_4^- = \frac{u_{i+3/2,j} - u_{i+1/2,j}}{\Delta x},$$
$$q_5^- = \frac{u_{i+5/2,j} - u_{i+3/2,j}}{\Delta x}$$

and

$$q_1^+ = \frac{u_{i+7/2,j} - u_{i+5/2,j}}{\Delta x}, \quad q_2^+ = \frac{u_{i+5/2,j} - u_{i+3/2,j}}{\Delta x}, \quad q_3^+ = \frac{u_{i+3/2,j} - u_{i+1/2,j}}{\Delta x}, \quad q_4^+ = \frac{u_{i+1/2,j} - u_{i-1/2,j}}{\Delta x},$$
$$q_5^+ = \frac{u_{i-1/2,j} - u_{i-3/2,j}}{\Delta x}.$$

The weights $\omega_k^\pm$ are chosen such that the smoothest ENO3 stencil is given the most significant contribution to the approximation; thus, any sharp discontinuity in the solution is given minimal weight reducing the numerical errors and potential instabilities. Omitting the superscript $\pm$, the weights are written as

$$\omega_1 = \frac{\alpha_1}{\alpha_1+\alpha_2+\alpha_3}, \quad \omega_2 = \frac{\alpha_2}{\alpha_1+\alpha_2+\alpha_3} \quad \text{and} \quad \omega_3 = \frac{\alpha_3}{\alpha_1+\alpha_2+\alpha_3},$$

where

$$\alpha_1 = \frac{0.1}{(S_1+\epsilon)^2}, \quad \alpha_2 = \frac{0.6}{(S_2+\epsilon)^2} \quad \text{and} \quad \alpha_3 = \frac{0.3}{(S_3+\epsilon)^2},$$

with the regularization parameter $\epsilon = 10^{-6}$ and the smoothness indicators S_k given by

$$S_1 = \frac{13}{12}(q_1 - 2q_2 + q_3)^2 + \frac{1}{4}(q_1 - 4q_2 + 3q_3)^2,$$
$$S_2 = \frac{13}{12}(q_2 - 2q_3 + q_4)^2 + \frac{1}{4}(q_2 - q_4)^2,$$
$$S_3 = \frac{13}{12}(q_3 - 2q_4 + q_5)^2 + \frac{1}{4}(3q_3 - 4q_4 + q_5)^2.$$

In smooth regions, where all S_k are approximately the same size, all three approximations are given the weighting such that optimal fifth order accuracy is obtained. In non-smooth regions the accuracy of the WENO scheme reduces to third order only; same as the ENO3 scheme.

The first-derivative in the y-direction, $(u_y)_{i+1/2,j}$, is obtained in a similar fashion where $v_{i+1/2,j}$ is used to determine the upwind direction.

To summarize, using the subset

$$\mathbb{D}_x = \{u_{i-5/2,j}, u_{i-3/2,j}, u_{i-1/2,j}, u_{i+1/2,j}, u_{i+3/2,j}, u_{i+5/2,j}, u_{i+7/2,j}\}$$

we can obtain numerical approximations to $(u_x)_{i+1/2,j}$ and $(u_{xx})_{i+1/2,j}$ following the procedure described above. Similarly, using the subset

$$\mathbb{D}_y = \{u_{i+1/2,j-3}, u_{i+1/2,j-2}, u_{i+1/2,j-1}, u_{i+1/2,j}, u_{i+1/2,j+1}, u_{i+1/2,j+2}, u_{i+1/2,j+3}\},$$

we can approximate $(u_y)_{i+1/2,j}$ and $(u_{yy})_{i+1/2,j}$ following the same procedure. These approximations are found straightforwardly since none of the velocity points in the subsets are separated by a surface element.

On the other hand, if the point of interest is located close to an immersed boundary such that at least one of the velocity points in the subsets above is separated from the rest by a surface element (see Fig. 6) some modifications are required in order to satisfy the boundary conditions correctly. Since all terms in the numerical discretization can be treated dimension by dimension it is simple to adopt the one-dimensional ghost cell approach described in Section 2. That means that any point separated by an immersed boundary can be replaced by a temporary, fictitious value which smoothly extends the solution across the boundary. For instance, as shown in Fig. 6, the velocities $u_{i+3/2,j}, u_{i+5/2,j}$ and $u_{i+7/2,j}$ cannot be used to evaluate $(u_x)_{i+1/2,j}$ and $(u_{xx})_{i+1/2,j}$ since the numerical discretizations are not valid across the boundary. However, if these velocities are replaced by a set of fictitious values, $u^g_{i+3/2,j}, u^g_{i+5/2,j}$ and $u^g_{i+7/2,j}$, obtained by extrapolating the solution along the x-direction, then $(u_x)_{i+1/2,j}$ and $(u_{xx})_{i+1/2,j}$ can be computed following the same procedure as above using the subset

$$\mathbb{D}^g_x = \{u_{i-5/2,j}, u_{i-3/2,j}, u_{i-1/2,j}, u_{i+1/2,j}, u^g_{i+3/2,j}, u^g_{i+5/2,j}, u^g_{i+7/2,j}\},$$

instead of $\mathbb{D}_x$. In a similar way, the derivatives $(u_y)_{i+1/2,j}$ and $(u_{yy})_{i+1/2,j}$ can be approximated using the subset

$$\mathbb{D}^g_y = \{u_{i+1/2,j-3}, u_{i+1/2,j-2}, u_{i+1/2,j-1}, u_{i+1/2,j}, u^g_{i+1/2,j+1}, u^g_{i+1/2,j+2}, u^g_{i+1/2,j+3}\},$$

where the ghost cell values $u^g_{i+1/2,j+1}, u^g_{i+1/2,j+2}$ and $u^g_{i+1/2,j+3}$ are obtained by extrapolation along the y-direction. Now, the x-component of Eq. (9) in the time-stepping procedure can be written as

$$\mathcal{F}_x(\mathbf{u}_{i+1/2,j}) = -(u_{i+1/2,j}(u_x)_{i+1/2,j} + v_{i+1/2,j}(u_y)_{i+1/2,j}) + \frac{1}{Re}((u_{xx})_{i+1/2,j} + (u_{yy})_{i+1/2,j}).$$

Likewise, we can obtain numerical approximations to $(v_x)_{i,j+1/2}, (v_y)_{i,j+1/2}, (v_{xx})_{i,j+1/2}$ and $(v_{yy})_{i,j+1/2}$ in similar manners as described above. Then the y-component of Eq. (9) becomes

$$\mathcal{F}_y(\mathbf{u}_{i,j+1/2}) = -(u_{i,j+1/2}(v_x)_{i,j+1/2} + v_{i,j+1/2}(v_y)_{i,j+1/2}) + \frac{1}{Re}((v_{xx})_{i,j+1/2} + (v_{yy})_{i,j+1/2}).$$

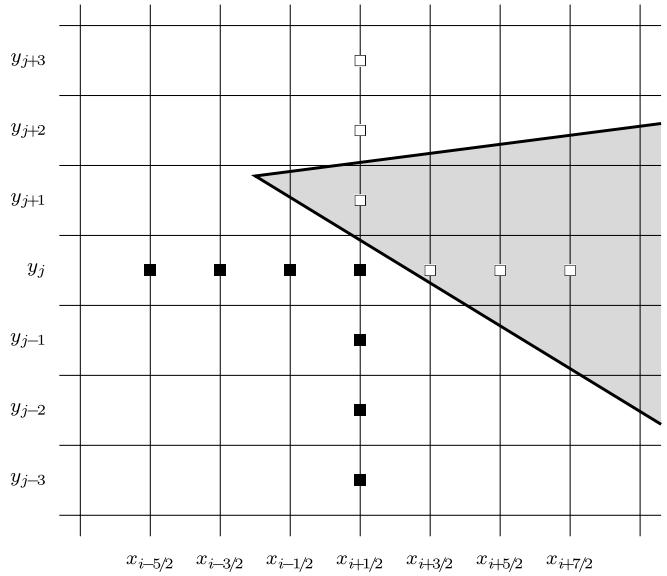

Fig. 6. The stencil for calculating $(u_x)_{i+1/2,j}$, $(u_{xx})_{i+1/2,j}$, $(u_y)_{i+1/2,j}$ and $(u_{yy})_{i+1/2,j}$. Invalid velocity points are replaced by fictitious ghost cell values (□) obtained by extrapolating active velocity points (■) across the immersed boundary.

As discussed in Section 2, the accuracy of the discretizations near the immersed boundary depends on the accuracy of the ghost cells. To preserve at least second order accuracy in the viscous terms it is necessary to use a cubic extrapolation scheme to obtain the ghost cell values; in this work a third order Lagrange polynomial is used. A cubic extrapolation scheme reduces the WENO scheme into a third order accurate ENO3 scheme near the immersed boundary since the three possible ENO3 schemes will in this case lie on the same curve. Further, if not enough active velocity points are available for a cubic extrapolation the order of the extrapolation scheme is reduced to conform to the nodes available. This will reduce the accuracy locally; however, the impact on the global accuracy is assumed to be negligible small since this situation is expected to occur at only a few places.

Velocity points located very close to the immersed boundary may be subject to numerical instabilities due to the singular behaviour of the extrapolation scheme. Considering the x-component of the momentum equation, the distance to the boundary in the x-direction for active velocity points must be at least half a grid cell spacing which limits the problem to the discretization in y-direction only. Therefore, if the distance to the immersed boundary along the y-direction is too small compared to the grid cell spacing, then the extrapolation scheme is modified as described in Section 2 in order to avoid any singular behaviour. Similarly, this is only a problem for the discretization in x-direction when solving the y-component of the momentum equation.

Furthermore, the cell centred velocity components cannot be calculated using simple averaging as in Eq. (16) if one of the velocity points involved is located on the other side of a boundary. In this case, a one-dimensional second order Lagrange polynomial, involving the boundary and two velocity points inside the flow, is used to reconstruct the cell centred velocity component. The cell face velocity components given by Eq. (17) are only evaluated in active velocity points; thus, the presence of an immersed boundary does not change the way they are calculated.

4.2.3. Discretization of the pressure Poisson equation

In order to advance the solution to a divergence-free velocity field at time t^{n+1} we need to solve a Poisson equation for the pressure. For a staggered grid arrangement we use an exact projection method: the discrete divergence constraint is exactly enforced. The projection step is performed twice, one for each step of the time-integration procedure. For brevity, since both projection steps are identical, we will only focus on the pressure Poisson Eq. (13) in the corrector step.

We try to find a pressure, $p_{i,j}$, such that the following constraint is satisfied

$$\nabla \cdot \mathbf{u}_{i,j}^{n+1} = 0, \tag{18}$$

at every active grid cell where the divergence operator is defined by the central scheme

$$\nabla \cdot \mathbf{u}_{i,j}^{n+1} = \frac{u_{i+1/2,j}^{n+1} - u_{i-1/2,j}^{n+1}}{\Delta x} + \frac{v_{i,j+1/2}^{n+1} - v_{i,j-1/2}^{n+1}}{\Delta y}. \tag{19}$$

For regular grid cells, where all the surrounding velocity points are active, using Eq. (12) we can write

$$\begin{aligned}
u_{i+1/2,j}^{n+1} &= u_{i+1/2,j}^{**} - \Delta t\left(\frac{p_{i+1,j} - p_{i,j}}{\Delta x}\right),\\
u_{i-1/2,j}^{n+1} &= u_{i-1/2,j}^{**} - \Delta t\left(\frac{p_{i,j} - p_{i-1,j}}{\Delta x}\right),\\
v_{i,j+1/2}^{n+1} &= v_{i,j+1/2}^{**} - \Delta t\left(\frac{p_{i,j+1} - p_{i,j}}{\Delta y}\right),\\
v_{i,j-1/2}^{n+1} &= v_{i,j-1/2}^{**} - \Delta t\left(\frac{p_{i,j} - p_{i,j-1}}{\Delta y}\right),
\end{aligned}$$

where ∇p is approximated by central differences. Inserted into Eq. (18) recovers the standard discrete Poisson equation (13) for pressure at regular cells,

$$\frac{p_{i+1,j} - 2p_{i,j} + p_{i-1,j}}{\Delta x^2} + \frac{p_{i,j+1} - 2p_{i,j} + p_{i,j-1}}{\Delta y^2} = \frac{1}{\Delta t}\left(\frac{u_{i+1/2,j}^{**} - u_{i-1/2,j}^{**}}{\Delta x} + \frac{v_{i,j+1/2}^{**} - v_{i,j-1/2}^{**}}{\Delta y}\right).$$

If the grid cell is irregular special care must be taken in order to satisfy the divergence-free velocity constraint. Again, we want to satisfy Eq. (18) using the central scheme (19) where inactive velocity points are replaced by fictitious values obtained by interpolation (note that an inactive velocity point is either obtained by interpolation or extrapolation, depending on the location of the boundary, but for simplicity we shall now refer to both procedures as interpolation). For instance, assume that $\mathbf{x}_{i+1/2,j}$ is an inactive velocity point and $\mathcal{I}$ is an interpolation scheme which recovers the fictitious value satisfying the no-slip boundary condition, i.e.

$$u_{i+1/2,j}^{n+1,g} = \mathcal{I}(u^{n+1}).$$

We can split the interpolation $\mathcal{I}$ into two parts, $\mathcal{I}_1$ and $\mathcal{I}_2$,

$$u_{i+1/2,j}^{n+1,g} = \mathcal{I}(u^{n+1}) = \mathcal{I}\left(u^{**} - \Delta t\frac{\partial p}{\partial x}\right) = \mathcal{I}_1(u^{**}) - \Delta t\mathcal{I}_2\left(\frac{\partial p}{\partial x}\right)$$

or

$$u_{i+1/2,j}^{n+1,g} = u_{i+1/2,j}^{**,g} - \Delta t\left(\frac{\partial p}{\partial x}\right)_{i+1/2,j}^{g},$$

where $u_{i+1/2,j}^{**,g}$ can be interpreted as a fictitious, tentative velocity and $(\partial p/\partial x)_{i+1/2,j}^{g}$ as a fictitious pressure gradient. The no-slip condition in the interpolation $\mathcal{I}$ is satisfied by setting the boundary conditions $u_\Gamma^{**} = u_\Gamma^{n+1}$ and $(\partial p/\partial x)_\Gamma = 0$ in $\mathcal{I}_1$ and $\mathcal{I}_2$, respectively (cf. Eq. (14)). The pressure gradient at an active velocity point is approximated by a central difference stencil using the pressures on both sides of the cell face; therefore, we can replace $\mathcal{I}_2$ with an interpolation scheme $\hat{\mathcal{I}}_2$ such that

$$\mathcal{I}_2\left(\frac{\partial p}{\partial x}\right) = \hat{\mathcal{I}}_2(p).$$

Further, we define a fictitious pressure $p_{i+1,j}^{g}$ such that

$$\left(\frac{\partial p}{\partial x}\right)_{i+1/2,j}^{g} = \frac{p_{i+1,j}^{g} - p_{i,j}}{\Delta x} \quad \text{or} \quad p_{i+1,j}^{g} = p_{i,j} + \Delta x\left(\frac{\partial p}{\partial x}\right)_{i+1/2,j}^{g}.$$

Then the Poisson equation (13) for pressure at the irregular cell can be written as

$$\frac{p^g_{i+1,j} - 2p_{i,j} + p_{i-1,j}}{\Delta x^2} + \frac{p_{i,j+1} - 2p_{i,j} + p_{i,j-1}}{\Delta y^2} = \frac{1}{\Delta t}\left(\frac{u^{**,g}_{i+1/2,j} - u^{**}_{i-1/2,j}}{\Delta x} + \frac{v^{**}_{i,j+1/2} - v^{**}_{i,j-1/2}}{\Delta y}\right),$$

where the constraint

$$p^g_{i+1,j} - p_{i,j} - \Delta x \hat{\mathcal{I}}_2(p) = 0$$

closes the system. This way, the discrete divergence constraint (18) will be exactly enforced at the irregular cell since $\mathcal{I}(u^{n+1}) = \mathcal{I}_1(u^{**}) - \Delta t \mathcal{I}_2(\partial p/\partial x)$.

The choice of interpolation stencil $\mathcal{I}$ depends on the location of the immersed boundary. If the inactive velocity point lies inside the fluid on the same side of the boundary as the cell centre, then it is treated as a boundary point where a weighted combination of one-dimensional Lagrange interpolation is used (see Eq. (15)). If the boundary separates the inactive velocity point from the cell centre, then the fictitious value is obtained by extending the solution across the boundary as described in Section 2, i.e. one-dimensional extrapolation in the direction of discretization. For example, using a quadratic Lagrange polynomial to reconstruct the solution along the x-direction in the example above gives

$$\mathcal{I}_1(u^{**}) = \frac{2}{a(a+1)} u^{n+1}_\Gamma + \frac{2(a-1)}{a} u^{**}_{i-1/2,j} - \frac{a-1}{a+1} u^{**}_{i-3/2,j}$$

and

$$\hat{\mathcal{I}}_2(p) = \frac{2}{a(a+1)} \frac{\partial p}{\partial x_\Gamma} + \frac{2(a-1)}{a}\left(\frac{p_{i,j} - p_{i-1,j}}{\Delta x}\right) - \frac{a-1}{a+1}\left(\frac{p_{i-1,j} - p_{i-2,j}}{\Delta x}\right),$$

where $a\Delta x$ is the distance between $\mathbf{x}_{i-1/2,j}$ and the immersed boundary. Subtracting $\Delta t \hat{\mathcal{I}}_2(p)$ from $\mathcal{I}_1(u^{**})$ recovers the quadratic interpolation

$$\mathcal{I}(u^{n+1}) = \frac{2}{a(a+1)} u^{n+1}_\Gamma + \frac{2(a-1)}{a} u^{n+1}_{i-1/2,j} - \frac{a-1}{a+1} u^{n+1}_{i-3/2,j},$$

since $(\partial p/\partial x)_\Gamma = 0$.

It is sufficient to use a quadratic Lagrange polynomial in order to preserve the second order accuracy of the discrete divergence operator; however, to ensure that the boundary points defined by Eq. (15) satisfy the discrete divergence constraint a cubic polynomial should be used for these points. This ensures that the updated velocity field actually satisfies both the no-slip boundary condition and the divergence constraint (18) at the end of the time step, as opposed to e.g. [1,14].

In general, this approach is adopted to all irregular grid cells where inactive velocity points are replaced by similar interpolation schemes. A set of additional constraints to p is coupled to the discrete Poisson equation in order to solve for the fictitious pressure cells created for irregular cells. The resulting system of linear equations can be solved using most types of iterative methods. We have successfully solved the linear system using the BiCGSTAB method with ILU(k) and ILUT preconditioning as provided in the SPARSKIT package [59,60].

4.3. Local grid refinement procedure

The local grid refinement approach adds new refinement grids to regions where the variations in the flow are expected to be high, e.g. in the boundary layer near solid surfaces. This local grid refinement is necessary in order to achieve required resolution and still maintain acceptable computational efficiency. The grid cells that are tagged for refinement are grouped together using the point clustering algorithm of [3] to form efficient block structured patches, or subgrids, which cover the tagged regions. These subgrids are refined and then tagged for further point clustering and refinement until adequate local resolution is obtained.

In a block structured approach, rectangular sub-domains are refined instead of individual grid cells such that regions where higher resolution is needed can be covered with a relatively small number of refined

subgrids (see Fig. 7). Although this approach results in some unnecessary refinement, the advantages are better efficiency of data access and less overhead costs due to irregular operations such as interlevel communications [50].

The refined subgrids are aligned with the underlying coarser grid. They form an hierarchical structure where the coarsest grid belongs to level $l = 0$ and the next finer grids belong to the next level $l = 1$, and so on. The refinement ratio between the two grid levels l and $l - 1$ is 2. The subgrids are properly nested, meaning that any refined grid communicate only with grids on same level l or with grids on only one refinement level higher $(l + 1)$ or lower $(l - 1)$. Any communication between two refinement levels l and $l + k$ where $k \geqslant 2$ goes through the intermediate levels. This simplifies the passing of information between the refinement levels.

The solutions at all refinement levels are fully coupled throughout the time-stepping procedure and all levels are given the same time step Δt. The finer grid solution is transferred from level $l + 1$ to the coarser level l in the overlap region by using simple averaging, starting from the finest level all the way down to the base grid at $l = 0$. Refined subgrids not extended to a physical boundary or another subgrid on same refinement level use information from coarser grids to provide boundary values. These boundary cells are updated by higher order interpolation on a coarser level.

4.3.1. The coarse/fine grid interface

Special attention must be given to the coarse/fine grid interface between two refinement levels when solving the pressure Poisson equation. Due to the staggered arrangement of the variables and the alignment of the refined grids, both the coarse level velocity and the fine level velocity are located at the grid interface. However, to ensure continuity across the grid interface, the velocity is calculated from the governing equations only on the fine level while the coarse level velocity is determined by linear interpolation of the fine grid velocity. Consequently, the coarse level pressure gradient at the grid interface also needs to be obtained from the fine level in a similar fashion in order to maintain a consistent pressure and velocity field.

We let the pressure on the coarse level act like a Dirichlet condition for the pressure on the fine grid level, while information is passed from the fine level to the coarse level through a non-homogeneous Neumann condition. This ensures that the pressure is continuous and smooth across the grid interface and is what [50] referred to as the *elliptic matching condition*.

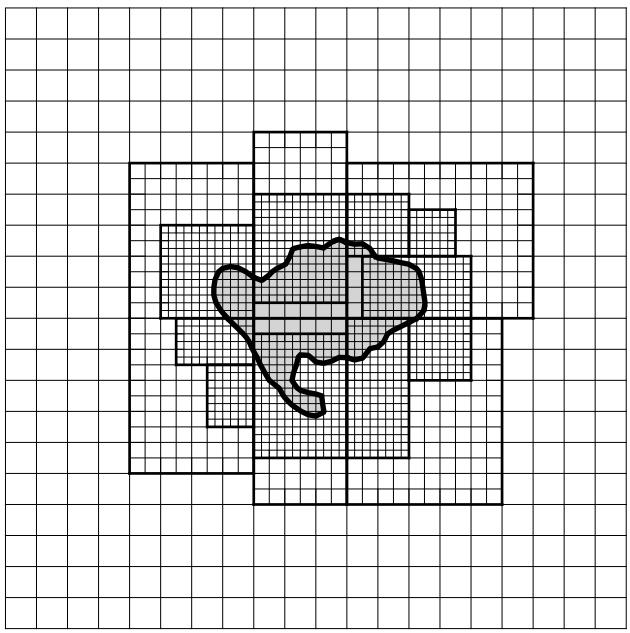

Fig. 7. Block structured grid refinement near the immersed boundary.

Following the approach of [50], we write the Laplace operator $\mathcal{L}(p) = \nabla^2 p$ in the pressure Poisson equation as a flux difference operator

$$\mathcal{L}(p)_{i,j} = \nabla \cdot \mathbf{f} = \frac{f^x_{i+1/2,j} - f^x_{i-1/2,j}}{\Delta x} + \frac{f^y_{i,j+1/2} - f^y_{i,j-1/2}}{\Delta y},$$

where the edge-based fluxes are given as $\mathbf{f} = \nabla p$. Let $\partial\Omega^{c/f}$ denote the boundary between the coarse and the fine computational domain.

For the region away from $\partial\Omega^{c/f}$, in both domains, the Laplace operator is the standard five point stencil where the edge-based fluxes are given as

$$f^x_{i+1/2,j} = \frac{p_{i+1,j} - p_{i,j}}{\Delta x} \quad \text{and} \quad f^y_{i,j+1/2} = \frac{p_{i,j+1} - p_{i,j}}{\Delta y}$$

in both directions. If the coarse cell is bordering the grid interface then the flux passing through $\partial\Omega^{c/f}$ is replaced by an average flux calculated on the fine grid level. For example, let coarse grid variables be denoted by capital letters and fine grid variables by small letters (see Fig. 8(a)) then summing the fluxes passing in and out of the coarse cell (I,J) located above the grid interface gives

$$\mathcal{L}(P)_{I,J} = \frac{F^x_{I+1/2,J} - F^x_{I-1/2,J}}{\Delta X} + \frac{F^y_{I,J+1/2} - F^{y,\text{ave}}_{I,J-1/2}}{\Delta Y},$$

where

$$F^x_{I+1/2,J} = \frac{P_{I+1,J} - P_{I,J}}{\Delta X}, \quad F^x_{I-1/2,J} = \frac{P_{I,J} - P_{I-1,J}}{\Delta X}, \quad F^y_{I,J+1/2} = \frac{P_{I,J+1} - P_{I,J}}{\Delta Y},$$

and

$$F^{y,\text{ave}}_{I,J-1/2} = \frac{1}{2}\left(f^y_{i,j-1/2} + f^x_{i+1,j-1/2}\right) = \frac{1}{2}\left(\frac{p_{i,j} - p_{i,j-1}}{\Delta y} + \frac{p_{i+1,j} - p_{i+1,j-1}}{\Delta y}\right).$$

The boundary cell values $p_{i,j}$ and $p_{i+1,j}$ are obtained by first a quadratic interpolation parallel to the boundary to get the intermediate points on both sides of the coarse grid node location as shown in Fig. 8(b). Then quadratic interpolations are used normal to the grid interface to get the boundary cell values for the fine grid. For the fine cells $(i, j-1)$ and $(i+1, j-1)$ adjacent to the grid interface, the Laplace operator $\mathcal{L}$ becomes the

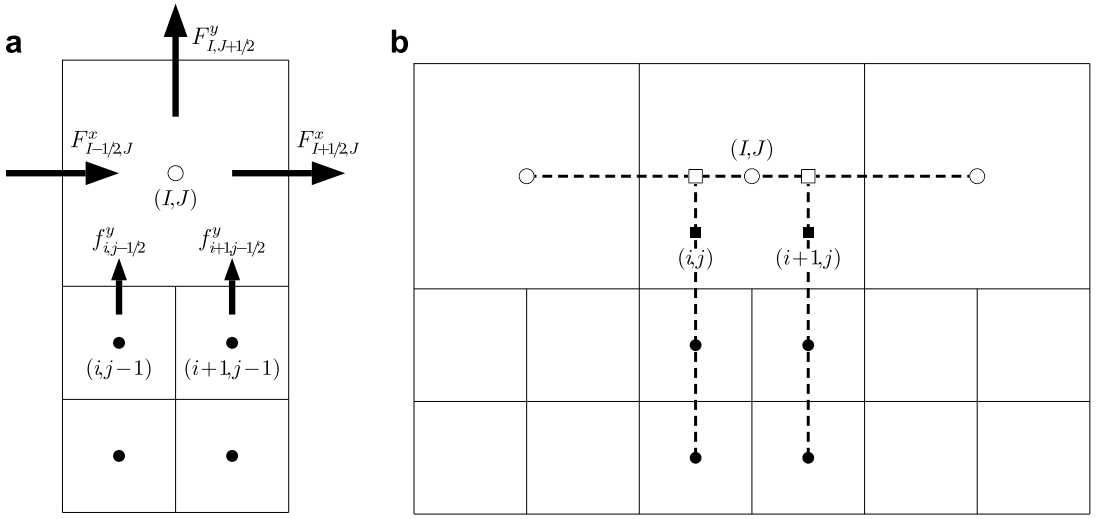

Fig. 8. (a) Coarse cell fluxes at the coarse/fine grid interface. (b) The interpolation stencil at the coarse/fine grid interface. Coarse cells (○); intermediate values on coarse grid (□); fine cells (●); boundary cells (■) for computing of coarse/fine fluxes.

standard five point stencil using the boundary cell values $p_{i,j}$ and $p_{i+1,j}$ since this is equivalent to enforcing the elliptic matching condition at $\partial\Omega^{c/f}$.

4.4. A few comments on moving boundaries

Although the focus of this work is on fixed boundaries only, there is nothing wrong in extending the present method to moving boundaries in the same fashion as many other immersed boundary methods. However, a few comments are found to be in place.

As the boundaries move across the grid, computational cells inside the solid (or located on one side of a thin body) at one time step may emerge into the fluid (or appear on the other side of the body) at the next one. These computational cells contain no correct time history of the velocity field and special treatment is necessary in order to evolve the solution to the next time level. One way is to treat all new velocity points in the same way as boundary points are treated, i.e. interpolating between active velocity points and the immersed boundary. This will require interpolation of the pressure gradient as well when solving the pressure equation. Alternatively, the tentative velocity at these new points can be obtained by extrapolating values from the flow field without involving the immersed boundary. In that case, the pressure equation can be solved without any special care regarding the newly emerged grid cells.

Another important challenge is related to the change of the discrete operators as the boundary moves. For instance, the right hand side of the pressure equation (13) will not necessarily change smoothly in time. This may result in large fluctuations in the pressure field from one time step to an other. For a moving circular cylinder with a relatively small time step a rather smooth change in the time evolution of $\nabla \cdot \mathbf{u}^{**}$ can be expected; however, that is not the case for sharp corners where the discrete operators may change abruptly from one time step to the next.

5. Numerical results

5.1. Numerical accuracy

The spatial accuracy of the present method is demonstrated by a grid refinement study for a lid-driven cavity containing a circular cylinder. The cavity, shown in Fig. 9(a), is a square box of height H where the cylinder is located at the centre of the cavity with diameter $D = H/2$. The horizontal velocity at the top lid is given a parabolic profile such that the velocity is maximum at the centre and zero at the corners. The Reynolds

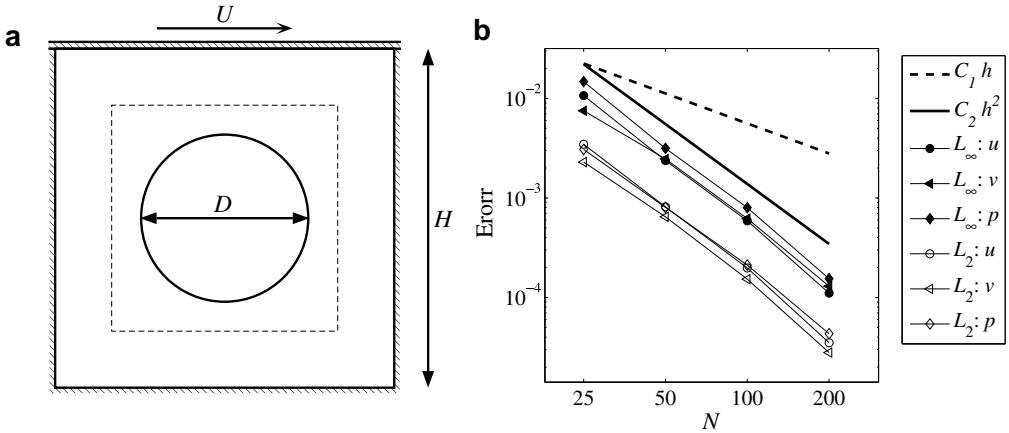

Fig. 9. Numerical accuracy: (a) the lid-driven cavity containing a cylinder. The dashed line box shows the bounded area for error calculations. (b) The convergence behaviour of the error norms for the velocity components u and v and pressure p. Solid symbols represent the L_∞ norm and open symbols represent the L_2 norms. The reference lines $C_1 h \sim \mathcal{O}(h)$ and $C_2 h^2 \sim \mathcal{O}(h^2)$ correspond to error norms with first and second order convergence rate, respectively.

number, based on the mean lid velocity and cavity height, is set equal to $Re = 100$. This example is similar to the test case used by [35], except a higher Reynolds number is used in this study.

Five different, uniformly spaced, grids are used for the error analysis. The number of grid points on each grid are 25^2, 50^2, 100^2, 200^2 and 400^2, respectively, where the finest grid solution is considered to be the benchmark solution. The same time step ($\Delta tU/H = 0.001$) is used for all grids in order to minimize the effect of temporal errors on the grid refinement analysis. The motion of the top lid is initiated impulsively and the simulations are carried out for 10 000 time steps. At the end of the simulations, the errors of the four coarser grids are quantified as the L_∞ and L_2 norms given by

$$\|E_N\|_\infty = \max_{i=1,n_p^N} |\phi_i^N - \phi_i^e| \quad \text{and} \quad \|E_N\|_2 = \left(\frac{1}{n_p^N} \sum_{i=1}^{n_p^N} |\phi_i^N - \phi_i^e|^2 \right)^{1/2},$$

respectively. Here, ϕ_i^N denotes a generic flow variable (e.g. velocity components u and v and pressure p) calculated on a $N \times N$ grid, n_p^N denotes the number of active points, and ϕ_i^e is the 'exact' solution obtained by interpolating the benchmark solution onto the test grid. The errors are calculated only inside the square box of size $2H/3$ surrounding the cylinder. This is to ensure that the error norms represent the actual error near the immersed boundary [35].

The results of the grid refinement analysis are summarized in Fig. 9(b). The error norms $\|E_N\|_\infty$ and $\|E_N\|_2$ for velocity components u and v and pressure p are plotted against the number of grid cells in each coordinate direction, N, in a log–log scale. Also plotted are the reference lines $C_1 h$ and $C_2 h^2$ corresponding to first and second order rate of convergence, respectively, where $h = 1/N$. The two constants C_1 and C_2 can be chosen arbitrarily, but for the best illustration of the convergence rate in Fig. 9(b) they are set equal to 0.28 and 3.45, respectively. It can be concluded that the rate of convergence is close to second order, since the slope of the error norms are close to the slope of $C_2 h^2$.

This conclusion can be further supported by the formula

$$\gamma = \frac{\log(\|E_{N/2}\|/\|E_N\|)}{\log(2)},$$

which approximates the order of accuracy γ such that $\|E_N\| \sim \mathcal{O}(h^\gamma)$, where $\|\cdot\|$ denotes an error norm. If $\gamma = 2$ then the rate of convergence is second order. Tables 1 and 2 show the rate of convergence for the L_∞ and L_2 norms, respectively. Apparently, both error norms exhibit approximately second order convergence, which reinforce our conclusion above.

Table 1
Rate of convergence calculated for the L_∞ norm

N	u		v		p	
	$\|E\|_\infty$	γ	$\|E\|_\infty$	γ	$\|E\|_\infty$	γ
25	1.067×10^{-2}		7.507×10^{-3}		1.473×10^{-2}	
50	2.370×10^{-3}	2.17	2.467×10^{-3}	1.61	3.148×10^{-3}	2.23
100	5.884×10^{-4}	2.01	6.197×10^{-4}	1.99	7.994×10^{-4}	1.98
200	1.107×10^{-4}	2.41	1.200×10^{-4}	2.37	1.544×10^{-4}	2.37

Table 2
Rate of convergence calculated for the L_2 norm

N	u		v		p	
	$\|E\|_2$	γ	$\|E\|_2$	γ	$\|E\|_2$	γ
25	3.462×10^{-3}		2.294×10^{-3}		3.071×10^{-3}	
50	8.136×10^{-4}	2.09	6.461×10^{-4}	1.83	8.023×10^{-4}	1.94
100	1.981×10^{-4}	2.04	1.529×10^{-4}	2.08	2.116×10^{-4}	1.92
200	3.514×10^{-5}	2.50	2.799×10^{-5}	2.45	4.331×10^{-5}	2.29

5.2. Uniform flow past a circular cylinder

In this section, the present method is used to compute uniform flow past a cylinder of circular cross section. Circular cylinders exposed to uniform flow has been widely investigated in the past and a large set of data is available for comparison. We examine the performance of the present approach for Reynolds numbers, based on the diameter D and the uniform far-field velocity U_∞, in the range 40–200. This includes flow in the steady, transitional and unsteady regime where the wake can be assumed to be laminar [64].

To ensure converged results it is necessary to perform a grid dependence study. Here we consider the sensitivity of the calculated drag and lift force due to variations in the grid resolution and domain size. Three different grids are used in the grid refinement study where the number of local grid refinement levels, $l_{\max}$, is equal to six. A systematic refinement procedure is used. That means the areas covered by patches of locally refined subgrids are fixed before all grid levels are refined subsequently by a factor of two. The base grid cell spacing on the coarsest grid is $\Delta x = \Delta y = 2D$. Also, the computational domain must be chosen sufficiently large such that the far field boundaries impose no noticeable effect on the flow. This effect is studied by changing the length and the width of the computational domain while holding the grid resolution near the cylinder fixed.

The computational domain can be described as follows: The cylinder is located at $(x, y) = (0, 0)$, a uniform inflow condition in the x-direction is prescribed at $x = -10D$, the top and bottom boundaries ($y = \pm y_{\max}$) are treated as free-slip walls, and homogeneous Neumann conditions ($\partial u/\partial x = 0$ and $\partial v/\partial x = 0$) are applied to the velocity field at the outflow boundary downstream of the cylinder at $x = x_{\max}$ where the outlet pressure is fixed as $p_{\text{outlet}} = 0$. The initial condition is the undisturbed uniform flow followed by an initial projection step in order to make the velocity satisfy the divergence constraint. In the case of unsteady flow the transition from a steady to an unsteady condition can be automatically initiated by computer round-off errors; however, to accelerate the transition to unsteady flow a small perturbation is imposed at the inflow boundary for a relatively short period of time.

Once the computed flow field has converged to a steady or periodic solution, it is possible to extract the time dependent drag and lift coefficients, defined as

$$C_{\mathrm{D}}(t) = \frac{F_{\mathrm{D}}(t)}{\frac{1}{2}\rho U_\infty^2 D} \quad \text{and} \quad C_{\mathrm{L}}(t) = \frac{F_{\mathrm{L}}(t)}{\frac{1}{2}\rho U_\infty^2 D},$$

respectively, where $F_{\mathrm{D}}(t)$ is the drag force and $F_{\mathrm{L}}(t)$ is the lift force. Further, the Strouhal number is defined as $St = fD/U_\infty$, where f is the vortex shedding frequency in the unsteady flow regime. The force $\mathbf{F} = (F_{\mathrm{D}}, F_{\mathrm{L}})$ is here calculated by direct integration of the pressure and the shear stresses along the immersed boundary, i.e.

$$\mathbf{F} = \int_\Gamma (-\mathbf{n}p + \mathbf{n}\cdot\tau)\mathrm{d}\Gamma, \tag{20}$$

where τ is the viscous stress tensor and $\mathbf{n}$ is the normal vector pointing into the fluid. An alternative way to calculate the force is to use the equations for conservation of linear momentum [15,80]. Let S_∞ by a fixed closed surface enclosing a control volume V and the immersed boundary. Then integrating the conservative form of the Navier–Stokes equation over the volume V and applying Gauss theorem we can show that

$$\mathbf{F} = \frac{\mathrm{d}}{\mathrm{d}t}\int_V \rho\mathbf{u}\,\mathrm{d}V + \int_{S_\infty} (\rho\mathbf{n}\cdot(\mathbf{u}\mathbf{u}) + \mathbf{n}p - \mathbf{n}\cdot\tau)\mathrm{d}S. \tag{21}$$

This expression is also referred to as the control-volume formulation [80].

Table 3 summarize the grid dependence study for $Re = 200$. The first three rows show the effect of varying the grid resolution on the Strouhal number, the time-averaged drag coefficient and the amplitude of the drag and lift coefficients. A reasonable approximation of the numerical error due to the grid resolution can be obtained by using Richardson extrapolation. The discretization error is estimated as [16]

$$\epsilon_h(\phi) = \frac{\phi_h - \phi_{2h}}{2^\gamma - 1}, \tag{22}$$

Table 3
Grid dependence study for uniform flow past a circular cylinder for $Re = 200$: Cylinder position $(x, y) = (0, 0)$, outlet position $x = x_{\max}$ and top and bottom boundaries $y = \pm y_{\max}$, minimum grid resolution near cylinder wall $\Delta x_{\min}$, Strouhal number St, drag coefficients C_{D}, m (mean) and C_{D}, a (amplitude), and lift coefficient $C_{\mathrm{L,a}}$ (amplitude)

Domain size		Grid		Results			
$x_{\max}$	$y_{\max}$	Base grid	$\frac{D}{\Delta x_{\min}}$	St	$C_{\mathrm{D,m}}$	$C_{\mathrm{D,a}}$	$C_{\mathrm{L,a}}$
$40D$	$15D$	25×15	32	0.19536	1.34721	0.04306	0.66824
$40D$	$15D$	50×30	64	0.19904	1.36656	0.04568	0.69598
$40D$	$15D$	100×60	128	0.19965	1.37020	0.04626	0.70040
$20D$	$7.5D$	30×15	128	0.20165	1.39039	0.04786	0.71587
$60D$	$22.5D$	70×45	128	0.19935	1.36829	0.04605	0.69717

The time step is equal to $\Delta t U_\infty / D = 0.0015$ and the number of grid refinement levels, $l_{\max}$, is 6.

where ϕ_h denotes the solution on a grid where $h = \Delta x = \Delta y$ is the base grid cell spacing. An approximation of the convergence rate is given by

$$\gamma = \frac{\log((\phi_{2h} - \phi_{4h})/(\phi_h - \phi_{2h}))}{\log(2)}.$$

It needs to be pointed out that Eq. (22) is only accurate if the grids are sufficiently fine such that monotone and nearly asymptotic convergence is obtained, the solution is well-behaved without singularities, and the grid refinement is systematic and substantial. The convergence rate for integral quantities, such as force coefficients, is usually the same as the theoretical order if the solution is smooth and well-behaved. For more complicated flows, a clear determination of the convergence rate may be difficult to obtain.

The results given in Table 3 converge monotonically towards a limiting value as the grid is refined. The estimated convergence rates for $C_{\mathrm{D,m}}, C_{\mathrm{D,a}}, C_{\mathrm{L,a}}$ and St are 2.41, 2.17, 2.65 and 2.60, respectively, which are close to the convergence rate obtained for the flow variables u, v and p in the previous example. Using Eq. (22) we may define the relative numerical error for a grid variable ϕ_h as $\bar{\epsilon}_h(\phi) = \epsilon_h(\phi)/(\phi_h + \epsilon_h(\phi))$. Then the relative error for $C_{\mathrm{D,m}}$ and $C_{\mathrm{L,a}}$ can be approximated to be about 0.06% and 0.12%, respectively, on the finest grid. The drag force amplitude coefficient $C_{\mathrm{D,a}}$ is somewhat more sensitive to the grid resolution, which is expected since $C_{\mathrm{D,a}} \ll C_{\mathrm{D,m}}$, where the relative error on the finest grid is about 0.36%. For the Strouhal number the approximated relative error on the finest grid is only 0.06%.

The force coefficients in Table 3 are based on Eq. (20). We may also use the control-volume formulation (21) to calculate the drag and lift force on the cylinder. This gives $C_{\mathrm{D,m}} = 1.37222$, $C_{\mathrm{D,a}} = 0.04638$ and $C_{\mathrm{L,a}} = 0.70097$ on the finest grid. We notice there is an acceptable agreement between the force coefficients obtained by both methods and, thus, the conservation of linear momentum is satisfactorily.

The effect of varying the size of the computational domain is demonstrated for the finest grid by the last three rows in Table 3. The size of the computational domain is given as $(10D + x_{\max}) \times (2y_{\max})$. We see that reducing the domain size to $30D \times 15D$ increases $C_{\mathrm{L,a}}$ by 2.2% and $C_{\mathrm{D,a}}$ by 3.5% as compared to the $50D \times 30D$ domain. Whereas increasing the domain size to $70D \times 45D$ change $C_{\mathrm{L,a}}$ and $C_{\mathrm{D,a}}$ by only 0.46% and 0.45%, respectively. Based on this grid dependence study it is found that the finest grid with the computational domain size $50D \times 30D$ capture the details of the two-dimensional laminar flow well, and it is used in the calculations below.

5.2.1. Steady case

The flow reaches a steady, symmetric state for Reynolds number equal to 40. Two attached, recirculating vortices are formed behind the cylinder as shown in Fig. 10 for the upper half of the symmetric flow. The length of the recirculation zone, the location of the vortex centres and the angle of separation is given in Table 4 where they are compared with experimental and other numerical results. Coutanceau and Bouard [11] evaluated experimentally the influence of blockage and extrapolated their data such that results for infinite fluid domain was presented. The present method predicts a somewhat larger recirculation zone than given by their extrapolated values, and the predicted horizontal location of the vortex centre is closer to the cylinder than obtained experimentally by [11]. The computed drag coefficient is also given in Table 4, and it is in reasonable

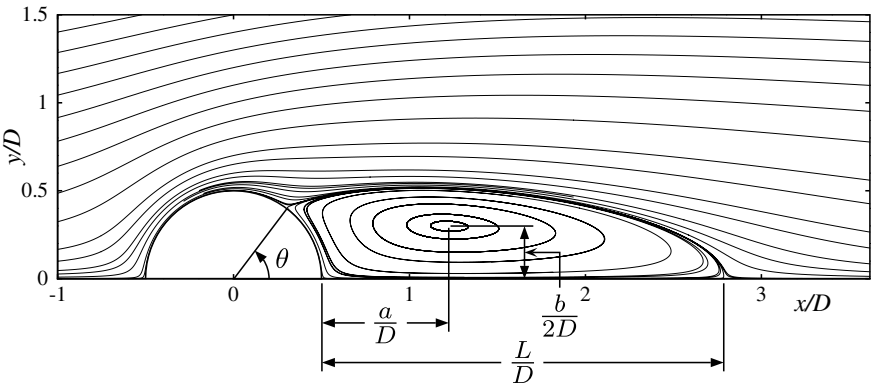

Fig. 10. The streamlines for $Re = 40$ and nomenclature used in Table 4.

agreement with the experimental value obtained by interpolating the results of [69]. Also, the present results are found to be within the range of values obtained by other numerical methods.

The drag coefficient can be split into two parts, $C_D = C_{Dp} + C_{Dv}$, one component due to pressure and one component due to viscous stresses, respectively. Henderson [26] showed that both C_{Dp} and C_{Dv} decrease as a function of Re in the steady regime, and he approximated his numerical results by simple functions involving only a two parameter fit (power law) where

$$C_{Dp}(Re) = 2.8676/Re^{0.2815} \quad \text{and} \quad C_{Dv}(Re) = 5.6106/Re^{0.64}.$$

For $Re = 40$ this give $C_{Dp} = 1.015$ and $C_{Dv} = 0.529$, which are close to but slightly below our calculated values of $C_{Dp} = 1.048$ and $C_{Dv} = 0.544$.

Fig. 11(a) compares the normalized wall pressure distribution with the experimental data of [24] and the numerical results of [12,70]. The normalized pressure coefficient is defined as $C_p = (p - p_\infty)/\frac{1}{2}\rho U_\infty^2$ where $p_\infty = 0$ is the ambient pressure. The calculated distribution of surface pressure agrees well with the experimental and numerical results. Using boundary layer approximations, Grove et al. [24] derived a theoretical expression for the stagnation pressure coefficient given as

$$C_{p_0} = 1 - \frac{v}{\frac{1}{2}U_\infty^2}\left.\frac{\partial u}{\partial x}\right|_{x=\delta,y=0} = 1 + \frac{A}{Re} + \cdots,$$

where δ is the boundary layer thickness and the constant $A = 8$ is obtained from the continuous potential solution. The stagnation pressure coefficient obtained from the simulation is $C_{p_0} = 1.24$ which is slightly larger than the theoretical value $C_{p_0} = 1.2$ for $Re = 40$. The distribution of vorticity on the cylinder surface is shown in Fig. 11(b). Our calculation compares well the numerical results of [8,12,70].

Table 4
Steady uniform flow past a circular cylinder for $Re = 40$: length L of recirculation zone, location (a, b) of vortex centre, separation angle θ, and drag coefficient C_D (nomenclature given in Fig. 10)

	L/D	a/D	b/D	θ (deg)	C_D
Coutanceau and Bouard [11][a]	2.13	0.76	0.59	53.5	–
Tritton [69][a]	–	–	–	–	1.57
Calhoun [9]	2.18	–	–	54.2	1.62
Le et al. [39]	2.22	–	–	53.6	1.56
Linnick and Fasel [45]	2.28	0.72	0.60	53.6	1.54
Russel and Wang [58]	2.29	–	–	53.1	1.60
Xu and Wang [81]	2.21	–	–	53.5	1.66
Herfjor [28]	2.25	0.71	0.60	51.2	1.60
Present study	2.29	0.72	0.60	53.9	1.59

[a] Experimental results. The experimental C_D value is obtained by interpolating the results of Tritton [69].

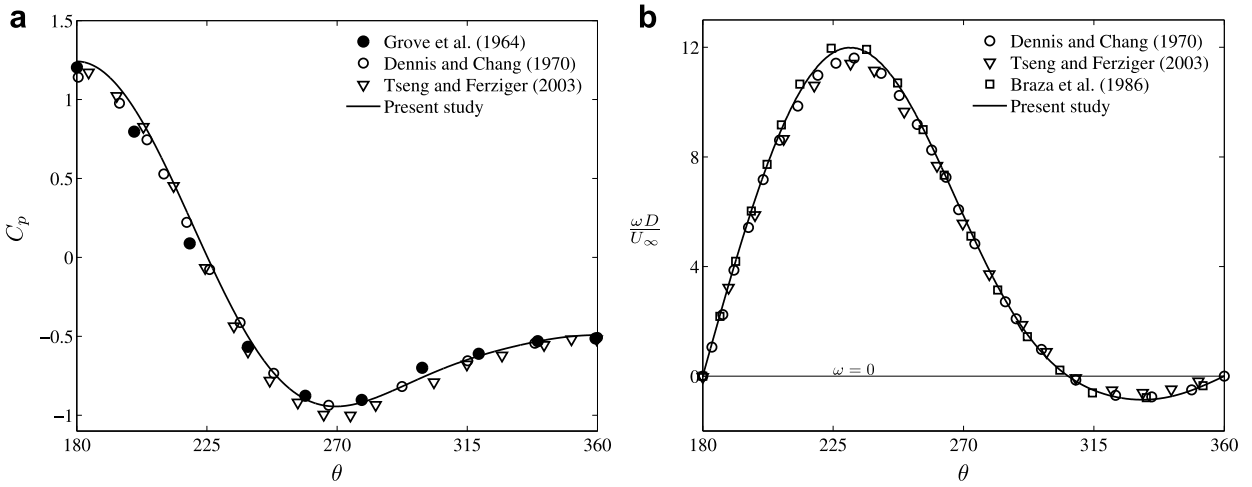

Fig. 11. Normalized (a) pressure and (b) vorticity distribution on the bottom half of the cylinder surface for $Re = 40$. The upstream stagnation point is located at $\theta = 180^\circ$ (nomenclature given in Fig. 10).

5.2.2. Unsteady case

The transition from steady to unsteady flow occurs at a critical Reynolds number between $Re = 40$ and 50. Above this critical value the symmetry of the flow breaks down and a periodic, alternating shedding of vortices from the cylinder wall occurs. To demonstrate the transition to this large scale 2D instability we consider the case $Re = 50$. In this example we do not impose a perturbation at the inflow boundary but instead let round-off errors in the computation trigger the instability. The time evolution of the lift coefficient is plotted in Fig. 12, where we see that the oscillations grow for a considerable long time before it stabilize around $tU_\infty/D = 2000$. This shows that the present method is fully capable of detecting the onset of vortex shedding, even with only an infinitesimal artificial disturbance of the flow caused by the round-off errors. At $tU_\infty/D = 2120$ we decrease the Reynolds number to $Re = 40$. Immediately, we notice how quickly the oscillations damp out and, eventually, vanish. This indicates that the onset of laminar vortex shedding occurs somewhere between these two Reynolds numbers, and it agrees with results found elsewhere (e.g. [26,39,45,58,61,69]).

The Strouhal number, which characterize the vortex shedding process, is estimated directly from the periodic variation of the lift coefficient. As long as the vortex shedding is regular, this is a preferred approach as

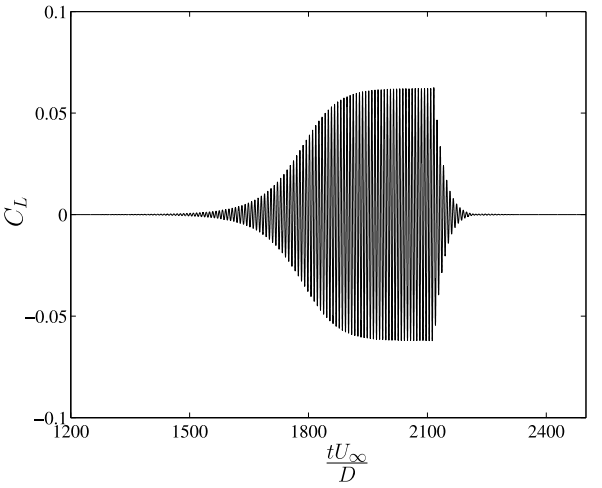

Fig. 12. Onset of laminar vortex shedding: Time evolution of the lift coefficient for $Re = 50$. Decreasing the Reynolds number to $Re = 40$ at $tU_\infty/D = 2120$ damps out the instability.

compared to using a discrete Fourier transform where a long sampling period of time is required in order to accurately determine the Strouhal number. Williamson [78] proposed an empirical relation between the parallel (2D) shedding frequency and the Reynolds number based on experimental data, where

$$St = 0.00016Re + 0.1816 - 3.3265/Re. \tag{23}$$

We obtained a Strouhal number equal to 0.128 for $Re = 50$ in the simulation above. This is about 4% higher than the empirical value $St = 0.123$. The calculated Strouhal numbers for $Re = 100$ and 200 are given in Table 5, where they are compared with experimental and numerical results. The computed St-values are 2.8% and 1.5% larger than the empirical ones for Reynolds numbers equal to 100 and 200, respectively. It should be noted that the flow undergoes a transition to three-dimensional shedding around $Re = 180$–194 [79,27] and there is a discontinuous drop in the Strouhal number as the wake vortices become unstable and generate large-scale vortex loops. Eq. (23) is therefore not truly valid for $Re = 200$; however, it gives a smooth continuation of the two-dimensional St–Re relation which is suitable for the purpose of comparison with two-dimensional numerical computations.

The time-averaged normalized pressure and vorticity distributions on the cylinder surface for Re equal to 100 and 200 are presented in Fig. 13. Our calculation compares well with the numerical results of [54] (as given in [34]) for $Re = 100$, but there is a larger discrepancy with the results presented by [34], particularly for ω near the location of maximum vorticity.

Table 5
Unsteady uniform flow past a circular cylinder for $Re = 100$ and 200: Strouhal number St, drag coefficients $C_{D,m}$ (mean) and $C_{D,a}$ (amplitude), and lift coefficient $C_{L,a}$ (amplitude)

	$Re = 100$				$Re = 200$			
	St	$C_{D,m}$	$C_{D,a}$	$C_{L,a}$	St	$C_{D,m}$	$C_{D,a}$	$C_{L,a}$
Williamson [78][a]	0.164	–	–	–	0.197	–	–	–
Calhoun [9]	0.175	1.33	0.014	0.298	0.202	1.17	0.058	0.668
Le et al. [39]	0.160	1.37	0.009	0.323	0.187	1.34	0.030	0.43
Linnick and Fasel [45]	0.166	1.34	0.009	0.333	0.197	1.34	0.044	0.69
Russel and Wang [58]	0.169	1.38	0.007	0.300	0.195	1.29	0.022	0.50
Xu and Wang [81]	0.171	1.42	0.013	0.34	0.202	1.42	0.04	0.66
Herfjord [28]	0.168	1.36	–	0.34	0.196	1.35	–	0.70
Present study	0.169	1.38	0.010	0.34	0.200	1.37	0.046	0.70

[a] Experimental results. The St-values are based on a least-squares curve fit to the experimental data given by Eq. (23).

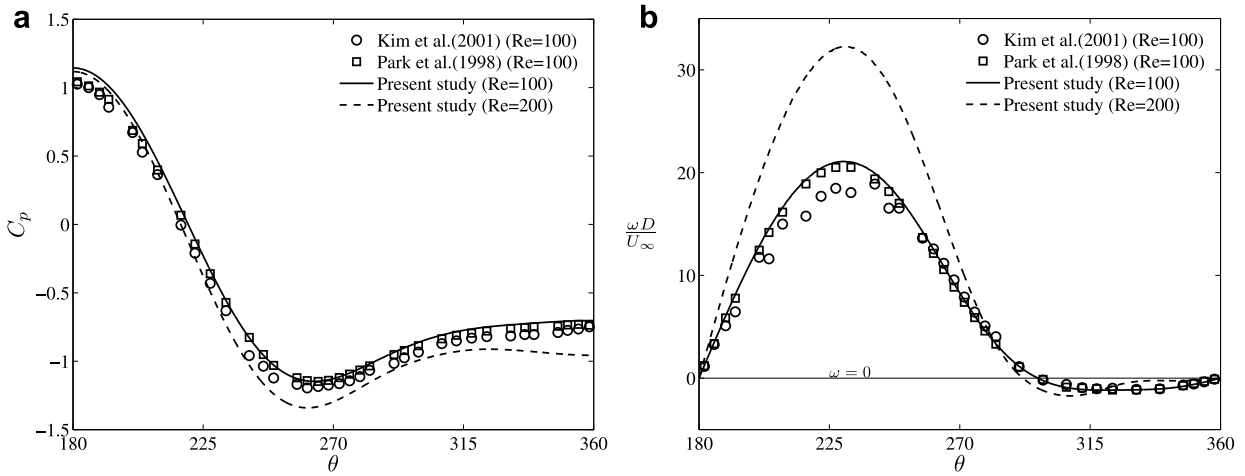

Fig. 13. Time-averaged normalized (a) pressure and (b) vorticity distribution on the bottom half of the cylinder surface for $Re = 100$ and 200. The upstream stagnation point is located at $\theta = 180^\circ$ (nomenclature given in Fig. 10).

The contribution from the pressure force, C_{Dp}, becomes increasingly important in the unsteady regime, but the skin friction, C_{Dv}, continues to drop as the Reynolds number is increased. This reduction in C_{Dv} balance the increase in C_{Dp} such that the total mean drag coefficient remains nearly constant. Henderson [26] fit his numerical results to the curves

$$C_{Dp,m}(Re) = 1.4114 - 0.2667Re^{0.1648}\exp(-3.375 \times 10^{-3}Re)$$

and

$$C_{Dv,m}(Re) = 2.5818/Re^{0.4369}$$

for the time-averaged force coefficients. In the present calculations we obtained $C_{Dp,m} = 1.028$ and $C_{Dv,m} = 0.349$ for Reynolds number equal to 100. The corresponding numbers obtained from the curve fit above are $C_{Dp,m} = 1.005$ and $C_{Dv,m} = 0.345$. For Reynolds number equal to 200 we obtained $C_{Dp,m} = 1.113$ and $C_{Dv,m} = 0.258$, and Henderson's [26] formula give $C_{Dp,m} = 1.086$ and $C_{Dv,m} = 0.255$. As for the steady case the deviation is slightly larger for the pressure force than the viscous force but in overall there is a reasonable agreement.

The drag and lift coefficients obtained for Reynolds numbers equal to 100 and 200 are also summarized and compared with other numerical results in Table 5. The results considered here are found to be within the range of data presented by others. However, there is a somewhat large scatter in the data reported, and this can be partly attributed to the difference in the computational setup, e.g. domain size, grid resolution, boundary conditions, and the nature of the numerical methods.

5.3. Impulsively started flow past objects

The impulsively started flow is here considered for a circular cylinder where $Re = 550$ and for a flat plate oriented normal to the flow where $Re = 126$.

5.3.1. A circular cylinder in impulsively started flow

Flow around a circular cylinder at a relatively large Reynolds number of 550 is known to eventually develop three-dimensional phenomena. However, at an early stage the flow will develop symmetrically about an axis through the centre of the cylinder in the flow direction and the wake will still be laminar and two-dimensional. The flow development is here considered only up to $tU_\infty/D = 3.0$. The computational setup is the same as in the previous example where the cylinder diameter is D, the height of the domain is $30D$ and the total length is $50D$. The initial condition is the undisturbed uniform flow with velocity U_∞ followed by an initial projection step in order to enforce the divergence constraint.

The instantaneous drag coefficient C_D at $tU_\infty/D = 1.0$ is given for different grid resolutions in Table 6. We notice that the difference in the drag coefficient obtained by the two finest grid resolutions is less than 0.3%. Also, as given in Table 6, reducing the time step to half the size changes the drag coefficient by only approximately 0.02%. Fig. 14 presents the normalized pressure coefficient and vorticity distribution on the cylinder surface together with the radial velocity profile on the symmetry axis behind the cylinder for different grid resolutions at $tU_\infty/D = 1.0$. There is no significant difference in the results produced by the two finest grid resolutions. We may conclude from this grid dependence study that the finest grid resolution with time step size $\Delta tU_\infty/D = 0.001$ is sufficiently fine for this example, and it is used in the results presented below.

Table 6
Grid dependence study for impulsively started flow past a circular cylinder at dimensionless time $tU_\infty/D = 1.0$: minimum grid resolution near cylinder wall Δx_{min}, drag coefficients C_D, time step Δt

$\frac{\Delta tU_\infty}{D}$	Base grid	$\frac{D}{\Delta x_{min}}$	C_D
0.001	50×30	64	1.14426
0.001	100×60	128	1.13403
0.001	200×120	256	1.13101
0.0005	200×120	256	1.13074

The number of grid refinement levels, l_{max}, is 6.

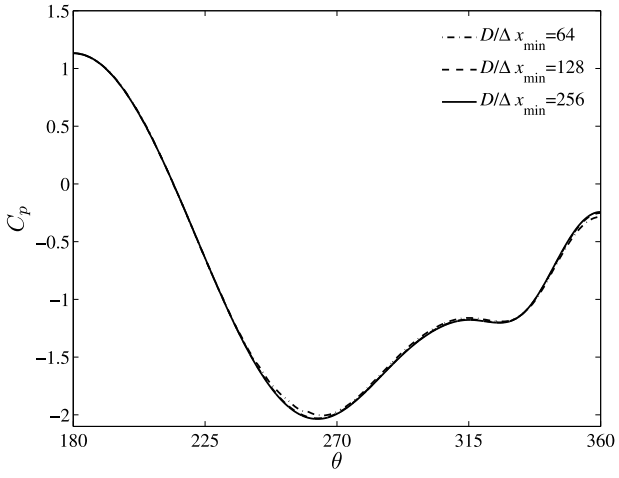

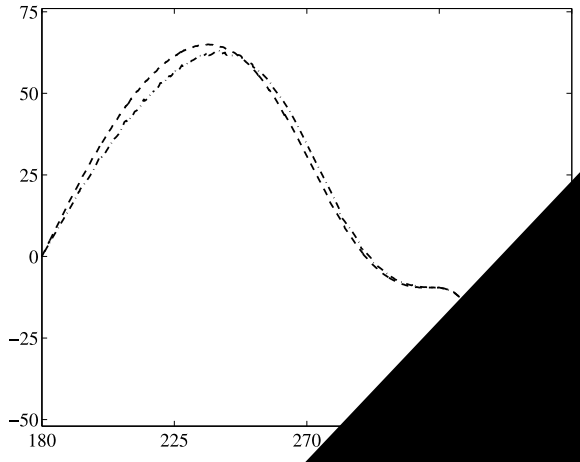

s the i
ir of smal
er wall, bounded b
th the experimental visual
s presented in [25,36,52,65].
development of the radial velocity profile on
The behaviour of the present results compare satisfact
mall discrepancy is found in the magnitude of the velocity. As sh
a somewhat lower magnitude of the maximum velocity, $|u_m|$, on the symm
ghtly shorter distance from the cylinder to the location of maximum magnitude, d_m, than
in the experiment [5]. It should be noted that in experiments the flow is not actually impulsively starte
quickly accelerated from zero to the given velocity. This partly explains the difference with the numerical predictions. The present calculations are also compared with the numerical results of [65] for the radial velocity along the symmetry line in Fig. 16(a).

The evolution of the wake length L and the location of the primary vortex centre (a, b) are given in Fig. 17. The present method predicts a shorter wake length than given by the experimental measurements [5] but

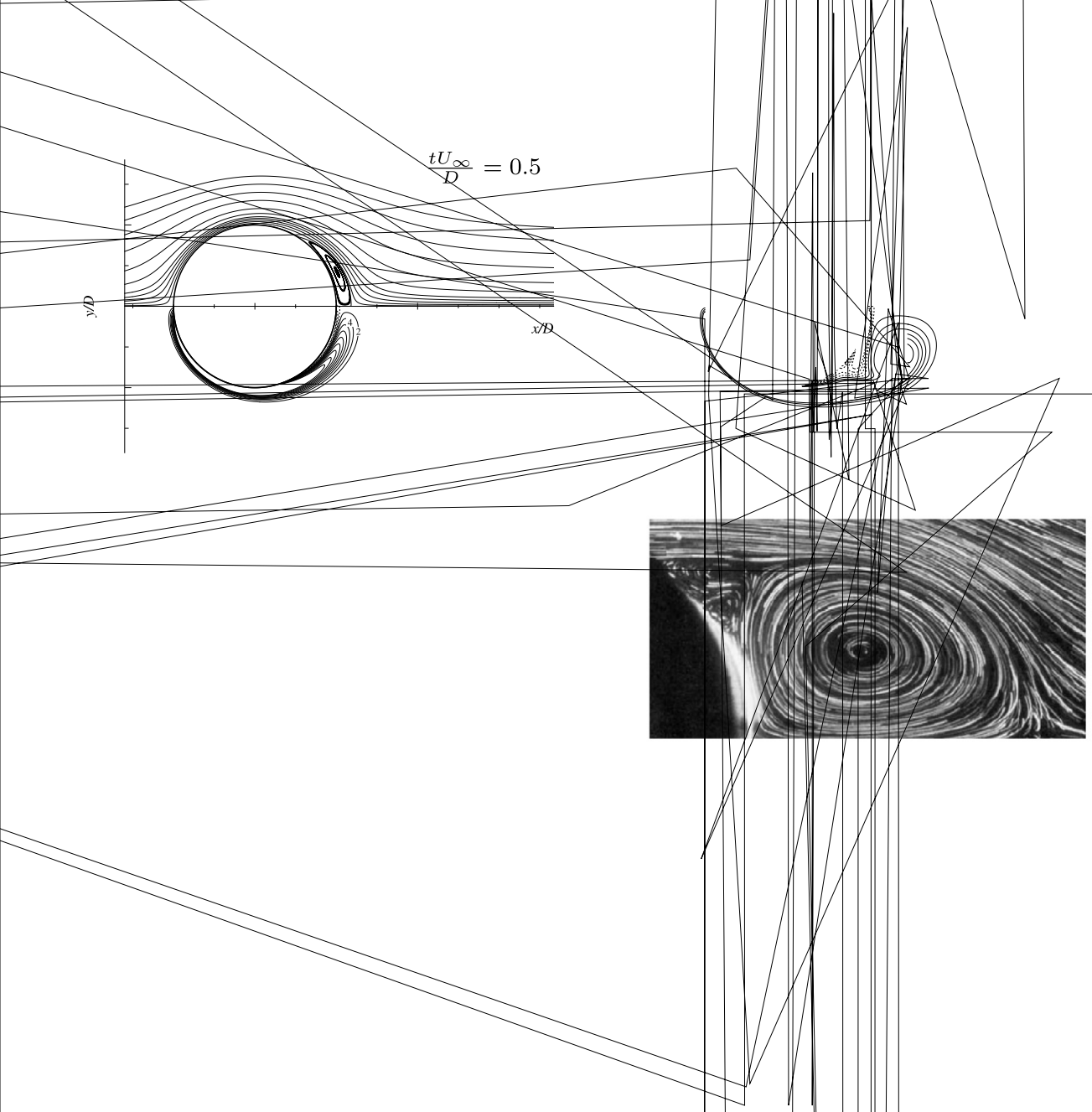

well with the numerical results of [65]. There is a reasonable agreement between the calculated and measured location of the vortex centre, although the predicted horizontal location is slightly closer to the cylinder.

The calculated instantaneous distribution of vorticity on the bottom half of the cylinder surface is compared with the numerical results of [36,52,65] in Fig. 18. The figure shows some scatter in the results but the overall behaviour is similar. We notice the points of zero vorticity, representing either separation

or re-attachment of the flow, as they appear on the cylinder surface. This clearly indicates the presence of an attached secondary vortex about 35–45° from the rear stagnation point followed by an evolving tertiary vortical region (as observed by [36,52]) in Fig. 18(b) and (c). We see from Fig. 14(b) and 18(b) that the secondary vortex appears sometime between $tU_\infty/D = 1.0$ and 1.5, which agrees with the time reported by [40,65].

5.3.2. A flat plate normal to an impulsively started flow

Next, we consider a flat plate in an impulsively started flow. The computational setup is identical to the previous example where the circular cylinder is replaced by an infinite thin plate oriented normal to the flow. The Reynolds number, which is equal to 126, is based on the height, D, of the plate and the uniform free stream velocity, U_∞.

Table 7 summarize the grid dependence study for the instantaneous drag coefficient at $tU_\infty/D = 1.0$. For the two finest grid resolutions, the difference in drag coefficient is less than 0.07%. Reducing the time step on the finest grid does not change the drag coefficient noticeably. Fig. 19(a) and (b) shows the normalized pressure and vorticity distribution, respectively, on the plate surface for different grid resolutions at $tU_\infty/D = 1.0$. There is virtually no difference in the results for the two finest grid resolutions except for close to the edges of the plate due to the nearly singular behaviour of the flow. This singularity seems to only have a local effect on the accuracy, and the area affected decreases as the grid is refined. It should be noted that the pressure and vorticity are evaluated on the midpoint of the piecewise linear elements which describes the plate geometry. The size of each element is proportional to the grid resolution. This means that the outermost point evaluated is much closer to the actual tip of the plate for the finest grid than what it is for a coarser grid such that the extremal value for a fine grid appears to be much larger than for a coarse grid. It is expected that the actual tip values of C_p and ω are larger than what they appear to be in the plot.

Fig. 19(c) shows the horizontal velocity profile on the symmetry axis behind the plate for different grid resolutions. The difference between the two finest grids is negligible small. The singular behaviour near the tips of the plate does not seem to have any significant influence on the accuracy of the flow far away from the tips. The finest grid is used in the calculations presented below where $\Delta tU_\infty/D = 0.0005$.

The time evolution of the wake length L is given in Fig. 20. The present calculation agrees well with the experimental measurement of [66] up to about $tU_\infty/D = 4$. At later times, our approach under predicts the experimental data, but it follows closely to the numerical results presented by [37]. According to [37], it is suspected that the deviation from the measurements is due to the occurrence of three-dimensional effects and the onset of asymmetry in the experiments.

Instantaneous streamlines based on the present calculations are compared with the streaklines of [66] in Fig. 21. The computational results are in close agreement with the experimental visualization. Also, the instantaneous streamlines and vorticity contours shown in Fig. 22 are in reasonable agreement with the numerical results presented by [37].

5.4. Objects in harmonically oscillatory flow

In the remaining part of this work we will apply the present technique to planar oscillatory flow around cylinders in infinite fluid. These problems are characterized by the Keulegan–Carpenter number $KC = U_A T/D$ and the Stokes parameter $\beta = Re/KC = D^2/\nu T$, where U_A and T are the velocity amplitude and period, respectively, of the ambient oscillating flow, D is the characteristic length scale, and ν is the kinematic viscosity.

Table 7
Grid dependence study for impulsively started flow past a flat plate oriented normal to the flow at dimensionless time $tU_\infty/D = 1.0$: minimum grid resolution near cylinder wall $\Delta x_{\min}$, drag coefficients C_D, time step Δt

$\frac{\Delta tU_\infty}{D}$	Base grid	$\frac{D}{\Delta x_{\min}}$	C_D
0.0005	25×15	32	3.04410
0.0005	50×30	64	3.06744
0.0005	100×60	128	3.06953
0.00025	100×60	128	3.06954

The number of grid refinement levels, $l_{\max}$, is 6.

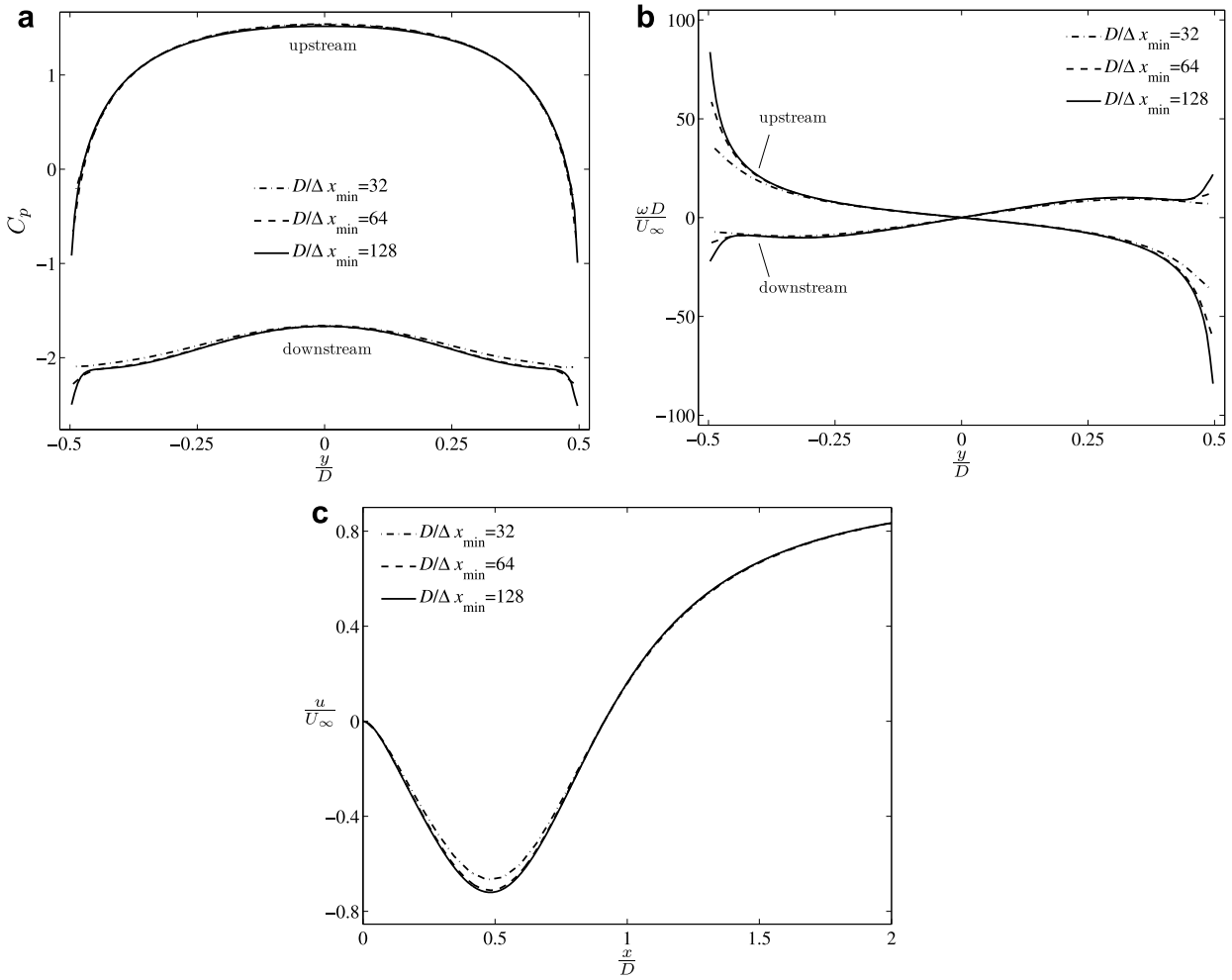

Fig. 19. Grid dependence study for impulsively started flow past a flat plate at dimensionless time $tU_\infty/D = 1.0$: (a) Normalized wall pressure distribution $C_p = (p - p_\infty)/\frac{1}{2}\rho U_\infty^2$ where $p_\infty = 0$, (b) normalized wall vorticity distribution, (c) normalized horizontal velocity profile on the symmetry axis behind the plate.

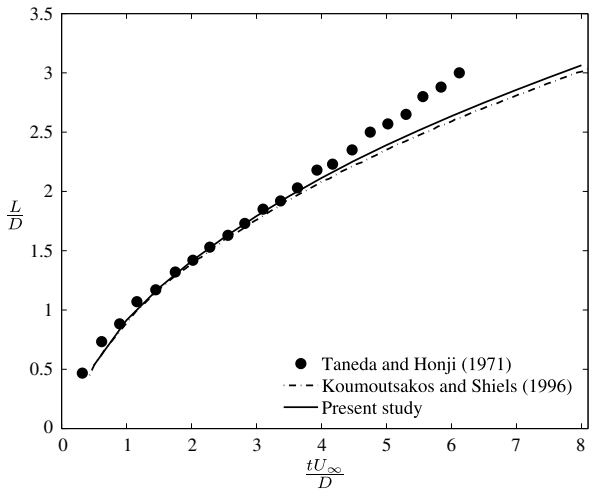

Fig. 20. Time evolution of the closed wake length L for a flat plate at $Re = 126$.

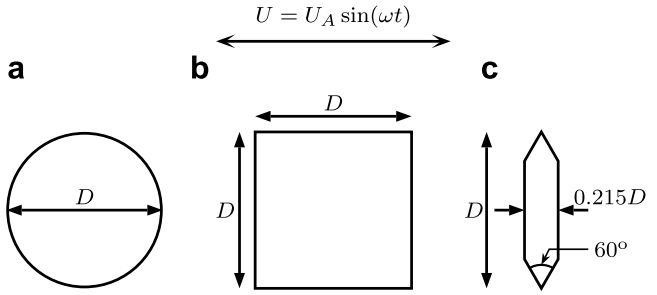

Fig. 23. Geometrical setup of objects in oscillatory flow. (a) A circular cylinder. (b) A facing square. (c) A chamfered plate.

obtained by adding the forces for an attached flow with a boundary layer and a separated flow based on a local vortex shedding model at each sharp edge of the cylindrical cross section. They presented an approximation to the force coefficient to the order $\mathcal{O}(\beta^{-1/2})$. Their approach is briefly outlined below.

If the Reynolds number is sufficiently large, the Keulegan–Carpenter number is small and the flow remains attached, then the flow can be described by an outer inviscid flow and an inner viscous laminar boundary layer. A first approximation of the outer inviscid flow can be analysed by neglecting the boundary layer. This potential flow contributes to a pressure force which is related to the acceleration of the fluid past the cylinder, and it can be expressed as

$$\frac{F_0}{\frac{1}{2}\rho U_A^2 D} = \frac{(\rho A_p + A_{11})}{\frac{1}{2}\rho U_A^2 D}\frac{\mathrm{d}U}{\mathrm{d}t} = \frac{(\rho A_p + A_{11})}{\rho D^2}\frac{4\pi}{KC}\cos\omega t,$$

where A_{11} is the added mass coefficient in the ambient flow direction and A_p is the cross sectional area.

The attached boundary layer is analysed by solving Stokes' second problem where we assume that the potential flow solution outside the boundary layer can be written as [15]

$$U_e(s,t) = U_o(s)\sin\omega t$$

for the local coordinate s along the cylinder surface. It is here assumed that the oscillatory amplitudes are small such that quadratic terms in the boundary layer equations can be neglected. The resulting non-dimensional force due to skin friction can then be written as

$$\frac{F_\mathrm{f}}{\frac{1}{2}\rho U_A^2 D} = \frac{2\sqrt{2}\pi}{KC\sqrt{\pi\beta}}\frac{1}{U_A D}\int_S U_o(s) n_x \,\mathrm{d}s \sin\left(\omega t + \frac{\pi}{4}\right),$$

where n_x is the directional cosine with respect to the x-axis. The theory gives zero force $F_{\mathrm{n}v}$ due to normal viscous stresses (this follows from the continuity equation). The boundary layer flow causes an outflow/inflow to the potential domain which influence the pressure. This effect on the streamwise force is equal to the contribution from the frictional force [2]. The total force due to the boundary layer can therefore be expressed as

$$\frac{F_\mathrm{BL}}{\frac{1}{2}\rho U_A^2 D} = \frac{2F_\mathrm{f}}{\frac{1}{2}\rho U_A^2 D} = \frac{4\sqrt{2}\pi}{KC\sqrt{\pi\beta}}\frac{1}{U_A D}\int_S U_o(s) n_x \mathrm{d}s \sin\left(\omega t + \frac{\pi}{4}\right).$$

The boundary layer approximation for general curved-wall flows is valid as long as the boundary layer thickness is small compared to the wall radius of curvature [80]. But this is not the case at a sharp edge as sharp edges invite immediate flow separation. Unless the separation effects on the body are confined to small regions near the edges then attached flow will not give an adequate prediction of the inviscid potential flow near the surface, and hence of the boundary-layer thickness $\delta_{99\%}$. Therefore, the predicted skin friction is likely to be in considerably error for these cases [2].

The final component of the streamwise force originate from the flow separation of the boundary layer leading to shedding of vortices. Bearman et al. [2] investigated only the effect of flow separation at sharp edges. For smooth, continuous surfaces, such as a circular cylinder, the flow will remain attached for KC numbers below a certain critical value depending on the Stokes parameter β and the shape of the body. On the other hand, the

flow will separate in the case of a sharp-edged cylinder even at low KC numbers. The shed vorticity is assumed to be concentrated in thin free shear layers, and the shedding at any edge is independent of the shedding at the other edges. The vortex shedding may be approximated by a discrete vortex method where the detailed boundary flow is neglected. Only the vorticity flux in the boundary layer at the separation point is needed. This is equal to half the square of the potential flow velocity at the separation point. However, there are potential errors due to the fact that a discrete vortex model is a numerical approximation of continuous thin free shear layers. The time rate of shed vorticity from a thin boundary layer into a thin free shear layer tends to be larger than in reality. The consequence is an overestimated drag force. Further, the effect of diffusion of vorticity in the free shear layer is neglected in such an approach.

5.4.1. A circular cylinder in oscillatory flow

The first example considered is a circular cylinder in infinite fluid. Numerical results are produced for KC numbers in the range 0.4–4. The Stokes parameter β is equal to 1035, which corresponds to the U-tube experiments of [62]. The cylinder's diameter is D, and it is located at the centre of the computational domain with the size $40D \times 40D$. The fluid is initially at rest. An oscillating inflow condition given by Eq. (25) is imposed at the left boundary, free-slip is applied at the top and bottom boundaries, and homogeneous Neumann conditions ($\partial u/\partial x = 0$ and $\partial v/\partial x = 0$) are used for the velocity components at the right boundary where the outlet pressure, p_{outlet}, is equal to zero. The flow is assumed to be symmetric for $KC \leqslant 2$ such that only the upper half of the computational domain is considered in the numerical computations.

The grid dependence study for KC equal to 2 is summarized in Table 8, where we consider the sensitivity of the calculated in-line force due to variations in the grid resolution, time step and domain size. The data presented are given for one oscillation period sampled from the tenth cycle. The in-line force is here represented by the drag and mass coefficients in Morison's equation. Three different grids are used in the grid refinement study where the number of refinement levels is eight. A systematic refinement procedure is used. The base grid cell spacing on the coarsest grid is $\Delta x = \Delta y = 2.5D$.

We notice from the first three rows of Table 8 that the force coefficients converge to a limiting value as the grid is refined. The variations are small as we go from the coarsest to the finest grid; however, the drag coefficient is more sensitive to the grid resolution than the mass coefficient. The difference between the two finest grids is about 2.1% for C_{D}, whereas the difference in C_{M} is only 0.066%. The reason for this is that the in-line force is nearly in phase with the acceleration of the fluid for low KC numbers such that Morison's equation is dominated by the mass term and, therefore, the extracted C_{D}-coefficient is very sensitive to even small errors in the force calculation.

A grid independent solution may be approximated by

$$\phi_0 = \phi_h + \epsilon_h(\phi), \tag{26}$$

where the numerical error ϵ_h is obtained using the Richardson extrapolation formula (22). Table 9 presents the calculated drag and mass coefficients obtained on the finest grid and the corresponding grid independent solutions for KC numbers in the range 0.4–2. The relative numerical error is about one magnitude larger for C_{D} than for C_{M}. It remains below 0.6% for C_{D} up to $KC = 1.7$, and it is about 1.2% for $KC = 2$. This sudden increase in the relative numerical error can be explained by the growing importance of flow separation and vortex shedding for larger KC numbers, which requires finer grid resolution further away from the cylinder

Table 8
Grid dependence study for harmonically oscillating flow past a circular cylinder for $\beta = 1035$ and $KC = 2$: oscillation period T, time step Δt, minimum grid resolution near cylinder wall $\Delta x_{\min}$, drag coefficients C_{D}, and mass coefficient C_{M}

Domain size	Time step	Grid		Results	
	$\frac{T}{\Delta t}$	Base grid	$\frac{D}{\Delta x_{\min}}$	C_{D}	C_{M}
$40D \times 20D$	2500	16×8	102.4	0.64669	2.03996
$40D \times 20D$	2500	32×16	204.8	0.61077	2.04374
$40D \times 20D$	2500	64×32	409.6	0.59797	2.04509
$40D \times 20D$	4000	64×32	409.6	0.59799	2.04509
$80D \times 20D$	2500	128×32	409.6	0.59796	2.04508

Table 9
Calculated force coefficients for a circular cylinder in oscillating flow where $\beta = 1035$: Drag coefficient $C_{D,h}$ and mass coefficient $C_{M,h}$ obtained on the finest grid, estimated grid independent drag coefficient $C_{D,0}$ and mass coefficient $C_{M,0}$, and the relative error $\bar{\epsilon}_h$

KC	$C_{D,h}$	$C_{D,0}$	$\bar{\epsilon}_h(C_D)$ (%)	$C_{M,h}$	$C_{M,0}$	$\bar{\epsilon}_h(C_M)$ (%)
0.4	2.10492	2.09651	−0.40	2.07029	2.07089	0.029
0.5	1.69429	1.68817	−0.36	2.07018	2.07078	0.029
0.7	1.23060	1.22646	−0.34	2.06978	2.07039	0.029
0.8	1.08837	1.08469	−0.34	2.06948	2.07008	0.029
1.0	0.89418	0.89089	−0.37	2.06858	2.06915	0.028
1.5	0.66025	0.65723	−0.46	2.06301	2.06344	0.021
1.7	0.61768	0.61413	−0.58	2.05834	2.05872	0.019
1.7[a]	0.61770	0.61409	−0.59	2.05834	2.05870	0.018
2.0	0.59797	0.59088	−1.20	2.04509	2.04583	0.037
2.0[a]	0.59802	0.59095	−1.20	2.04509	2.04580	0.035

[a] Means that numerical symmetry is not imposed.

surface in order to maintain the accuracy. But still, the predicted numerical errors are considered to be acceptable. We may also notice that imposing numerical symmetry has virtually no effect on the calculated force coefficients as shown in Table 9 for $KC = 1.7$ and 2.

Increasing the number of time steps per oscillation period to 4000 for the finest grid has no significant effect on the numerical results as shown in the fourth row of Table 8. This suggest that 2500 time steps per period should be sufficient in order to maintain a certain accuracy in the time-stepping procedure. Fewer steps per period was not possible as the time step was governed by numerical stability constraints on the finest grid making it necessary to keep the number of time steps per period equal to 2500. Extending the length of the computational domain does not influence the numerical results any noticeable as shown in the fifth row. It is therefore expected that the length of the computational domain is large enough for $KC \leqslant 2$.

For a circular cylinder we may write a first approximation of the potential flow solution outside the boundary layer as

$$U_e(\theta, t) = 2U_A \sin\theta \sin\omega t,$$

such that

$$\int_S U_o(s) n_x \, \mathrm{d}s = U_A D \int_0^{2\pi} \sin^2\theta \, \mathrm{d}\theta = U_A D \pi.$$

The non-dimensional frictional force in the ambient flow direction as obtained from the solution of Stokes' second problem may then be expressed as

$$\frac{F_\mathrm{f}}{\frac{1}{2}\rho U_A^2 D} = \frac{2\sqrt{2}\pi^2}{KC\sqrt{\pi\beta}} \sin\left(\omega t + \frac{\pi}{4}\right).$$

The comparison between this theory and our numerical calculations of the corresponding non-dimensional frictional force amplitude $C_{\mathrm{f,a}}$ is presented in Table 10. The boundary layer thickness can be estimated by [15,80]

$$\delta_{99\%} = 4.605\sqrt{\frac{2\nu}{\omega}} = \frac{4.605D}{\sqrt{\pi\beta}},$$

which gives $\delta_{99\%} = 0.081D$ when $\beta = 1035$. Although we can hardly claim that the examined case has a thin boundary layer, the agreement between the theoretical and numerical calculations of the frictional force amplitude seem to be good. The calculated non-dimensional force amplitude $C_{n\nu,\mathrm{a}}$ due to normal viscous stresses is also presented in Table 10. It should be noted that there are some uncertainties related to the calculated $C_{n\nu,\mathrm{a}}$ as the grid dependence study could not reveal a converged solution. Instead, the non-zero normal viscous force coefficient given in Table 10 is based on Richardson extrapolation. After all, the only purpose is to show that this component is negligible small compared to the skin friction, which coincides with the theoretical value of a

Table 10
Comparison of numerical and theoretical coefficients of frictional force amplitude $C_{f,a}$, normal viscous force amplitude $C_{nv,a}$, pressure force amplitude due to the boundary layer $C_{p,a}^{BL}$, and frictional force phase lead relative to the ambient flow velocity α_v

KC	Theory	Present			
	$C_{f,a}$	$C_{f,a}$	$C_{nv,a}$	α_v	$C_{p,a}^{BL}$
0.4	1.224	1.233	3.0×10^{-4}	0.775	1.241
0.5	0.979	0.988	2.6×10^{-4}	0.776	1.004
0.7	0.699	0.709	2.2×10^{-4}	0.776	0.739
0.8	0.612	0.622	2.1×10^{-4}	0.777	0.659
1.0	0.490	0.501	2.1×10^{-4}	0.778	0.552
1.5	0.326	0.342	2.3×10^{-4}	0.777	0.436
1.7	0.288	0.305	2.4×10^{-4}	0.776	0.422
2.0	0.245	0.266	2.7×10^{-4}	0.779	0.436

zero force due to normal viscous stresses. Since the normal velocity outside the boundary is not zero, the discretized expression for the normal derivative will most likely take a non-zero value and, hence, the calculated normal viscous stresses will not be exactly zero at the boundary. The theoretical frictional force phase lead relative to the ambient flow velocity α_v is $\pi/4 \approx 0.785$. As shown in Table 10, the numerically calculated value for α_v agrees well with the theoretical phase angle.

According to the theory, the streamwise pressure force due to the boundary layer is equal to the frictional force. Ignoring the effect of flow separation, we may extract the contribution to pressure force due to the boundary layer by considering the component of the pressure force which is in phase with the velocity. The non-dimensional pressure force amplitude due to the boundary layer $C_{p,a}^{BL}$ obtained from the numerical simulations are given in Table 10. We notice that there is close agreement between $C_{p,a}^{BL}$ and $C_{f,a}$ for $KC \leqslant 0.8$; however, these numbers are only approximate as, strictly speaking, there is a contribution to the pressure force due to flow separation which is in phase with the velocity. Although this contribution is small, it becomes more important as the Keulegan–Carpenter number is increased.

The added mass coefficient for a circular cylinder is $A_{11} = \rho\pi D^2/4$. Then, ignoring the possibility of flow separation, adding the contribution from the outer potential flow with the effect from the boundary layer gives the total streamwise force as

$$\frac{F_t}{\frac{1}{2}\rho U_A^2 D} = \left(\frac{2\pi^2}{KC} + \frac{4\pi^2}{KC\sqrt{\pi\beta}}\right)\cos\omega t + \frac{4\pi^2}{KC\sqrt{\pi\beta}}\sin\omega t.$$

In terms of Morison's equation (24), noting that $|\sin\theta|\sin\theta$ may be approximated by $(8/3\pi)\sin\theta$ over a flow cycle, the force coefficients can be expressed as

$$C_D = \frac{3\pi^3}{2KC}(\pi\beta)^{-1/2} \tag{27}$$

and

$$C_M = 2 + 4(\pi\beta)^{-1/2}. \tag{28}$$

Wang [76] investigated theoretically an oscillating circular cylinder in an otherwise still fluid using the method of inner and outer expansion. His analysis shows that for a stationary circular cylinder in oscillating flow we may write the drag and mass coefficients as

$$C_D = \frac{3\pi^3}{2KC}\left[(\pi\beta)^{-1/2} + (\pi\beta)^{-1} - \frac{1}{4}(\pi\beta)^{-3/2}\right] \tag{29}$$

and

$$C_M = 2 + 4(\pi\beta)^{-1/2} + (\pi\beta)^{-3/2}. \tag{30}$$

Wang's [76] solution is valid for $KC \ll 1, Re \cdot KC \ll 1$ and $\beta \gg 1$, primarily when the flow is two-dimensional, laminar and attached. Eqs. (29) and (30) differ from (27) and (28) only in the higher order terms $(\pi\beta)^{-1}$ and $(\pi\beta)^{-3/2}$. Both Stokes' and Wang's [76] solutions yield nearly identical results for large values

of β. Table 11 compares the drag coefficients for $\beta = 1035$ based on the present numerical calculation and the theoretical analyses for a selection of low KC numbers. The corresponding value for the theoretical mass coefficient C_M is 2.070. The numerically obtained drag coefficients are somewhat larger then the theoretical ones, but Wang's [76] result agree well with the numerical predicted drag coefficient at the lowest Keulegan–Carpenter numbers.

Calculated drag and mass coefficients are compared with theoretical [76] and experimental values [62] in Fig. 24. Both the numerical and experimental results follow the theoretical curves for small KC numbers until an abrupt deviation occurs for the measured drag coefficient at a critical Keulegan–Carpenter number $KC_{cr} \approx 0.7$. Experimental observations [62] showed that beyond this point an axially instability had occurred. This instability was observed by Honji [29] and later referred to as the Honji instability by Sarpkaya [62] which is a transition from a two-dimensional to a three-dimensional wake. The experimental drag coefficient remains nearly unchanged for KC numbers between 0.65 and 0.8, before it continues to drop parallel with the theoretical curve until a minimum drag is reached at $KC_{md} \approx 1.6$. According to Sarpkaya [62] C_D reaches its minimum value approximately when the boundary layer becomes turbulent ($KC_t \approx 1.7$). The numerically obtained C_D coefficient starts to deviate from the theoretical line near KC_{cr}. This deviation is not sudden nor as large as for the experimental data, which is anticipated as the Honji instability is a three-dimensional effect. The minimum drag occurs at $KC \approx 2$, which is somewhat later than observed in the experiment. The calculated C_M values agree well with theory for $KC < 2$, but they are slightly larger than the measured data.

The drag coefficient start to increase and the mass coefficient shows a small drop as KC continues to increase beyond the minimum drag. The effect of flow separation and vortex shedding become increasingly important for these Keulegan–Carpenter numbers, and the flow is now asymmetric and irregular. The force coefficients may undergo large variations from cycle to cycle and the characteristics of the flow may change even after a long time. The sampled data will be very sensitive to the time window they are collected from. Consequently, a long sampling period is necessary in order to get a statistically good representation of the

Table 11
Comparison of numerical and theoretical drag, C_D, for a circular cylinder, $\beta = 1035$

KC	C_D		
	Present	Stokes	Wang
0.4	2.097	2.039	2.075
0.5	1.688	1.631	1.660
0.7	1.226	1.165	1.186
1.0	0.891	0.816	0.830

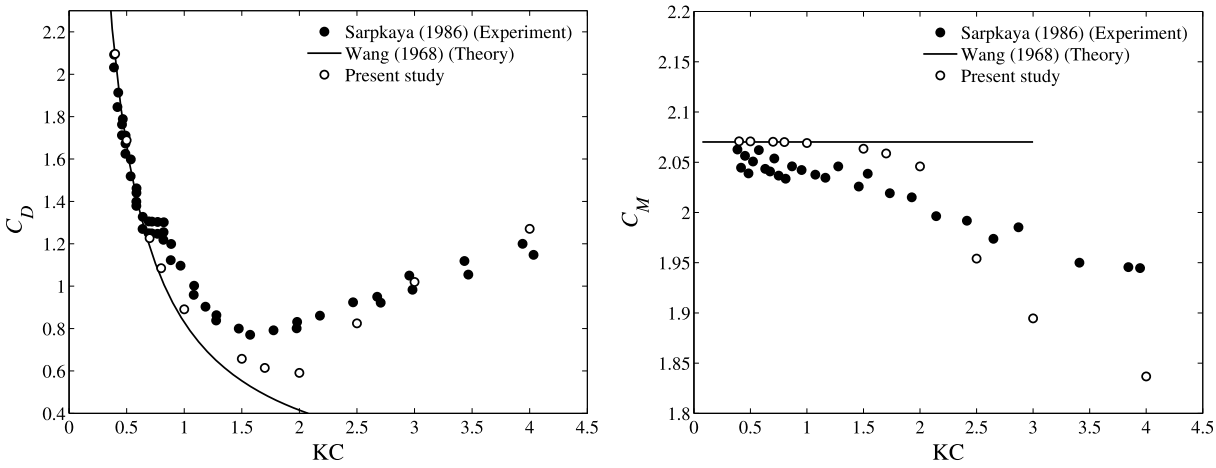

Fig. 24. Drag and mass coefficients for a circular cylinder in oscillating flow where $\beta = 1035$.

mean drag and mass coefficients. Therefore, a proper grid dependence study is not practical for large KC numbers, meaning that there is an increased uncertainty about the accuracy of the numerical results. However, transition to turbulence has already occurred at KC_{md}, and it is not expected that the numerical simulations should reproduce the experimental results correctly. The computational results for the higher Keulegan–Carpenter numbers are merely included in order to illustrate that we do obtain a nearly similar tendency from the two-dimensional laminar calculations as found in the measurements.

5.4.2. A facing square section in oscillatory flow

Next, we consider a square section in infinite fluid facing the flow direction. Numerical results are produced for Keulegan–Carpenter number in the range 0.1–4 with $\beta = 213$. The computational setup is similar to the one used for the circular cylinder where the width of the square section is D. We assume the flow is symmetric for $KC \leqslant 1.5$.

Three different grids are used in the grid dependence study. The number of refinement levels is equal to 7, where the base grid cell spacing is $\Delta x = \Delta y = 2D$ on the coarsest grid. The number of time steps per period is restricted by the numerical stability constraints on the finest grid, and it is here equal to 2500 steps per period. The data presented are sampled from the twentieth oscillation cycle, where we expect the flow to have reached a nearly stationary periodic state. Table 12 shows that the drag and mass coefficients for $KC = 1.5$ converge monotonically as the grid is refined. For the same reason as for the circular cylinder, the drag coefficient is more sensitive to the grid resolution than the mass coefficient. The difference is about 2.8% for C_{D} obtained on the two finest grids. The corresponding difference for C_{M} is only 0.11%. The calculated drag and mass coefficients obtained on the finest grid are presented in Table 13 for $KC \leqslant 1.5$ together with the corresponding grid independent solution estimated by the Richardson extrapolation (see Eq. (26)). The predicted numerical error is low for the smallest KC numbers. However, it grows up to about 1.6% for the drag coefficient at $KC = 1.5$. This increase is due to the growing importance of flow separation for larger KC numbers. Nevertheless, the error remains low for C_{M}, and since the in-line force is dominated by the mass term in Eq. (24) we consider the accuracy to be acceptable. Also, introducing numerical symmetry does not influence the result any significantly as demonstrated for $KC = 1.2$ and 1.5 in Table 13.

Table 12
Grid dependence study for harmonically oscillating flow past a facing square for $\beta = 213$ and $KC = 1.5$: oscillation period T, time step Δt, minimum grid resolution near cylinder wall $\Delta x_{\min}$, drag coefficients C_{D}, and mass coefficient C_{M}

Domain size	Time step	Grid		Results	
	$\frac{T}{\Delta t}$	Base grid	$\frac{D}{\Delta x_{\min}}$	C_{D}	C_{M}
$40D \times 20D$	2500	20×10	64	3.84627	3.06308
$40D \times 20D$	2500	40×20	128	3.57184	3.05495
$40D \times 20D$	2500	80×40	256	3.47301	3.05153

Table 13
Calculated force coefficients for a facing square in oscillating flow where $\beta = 213$: Drag coefficient $C_{\mathrm{D},h}$ and mass coefficient $C_{\mathrm{M},h}$ obtained on the finest grid, estimated grid independent drag coefficient $C_{\mathrm{D},0}$ and mass coefficient $C_{\mathrm{M},0}$, and the relative error $\bar{\epsilon}_h$

KC	$C_{\mathrm{D},h}$	$C_{\mathrm{D},0}$	$\bar{\epsilon}_h(C_{\mathrm{D}})$ (%)	$C_{\mathrm{M},h}$	$C_{\mathrm{M},0}$	$\bar{\epsilon}_h(C_{\mathrm{M}})$ (%)
0.1	24.3659	24.3592	−0.028	2.99464	2.99523	0.020
0.2	12.4959	12.4903	−0.045	2.99405	2.99469	0.022
0.5	5.68986	5.67969	−0.18	2.99335	2.99335	0.0
0.7	4.50029	4.48453	−0.35	2.99739	2.99693	−0.015
1.0	3.68165	3.65560	−0.71	3.01260	3.01027	−0.077
1.2	3.45594	3.42076	−1.03	3.02685	3.02314	−0.12
1.2[a]	3.45749	3.42198	−1.04	3.02694	3.02314	−0.13
1.5	3.47301	3.41737	−1.63	3.05153	3.04905	−0.082
1.5[a]	3.47417	3.41827	−1.64	3.05163	3.04909	−0.083

[a] Means that numerical symmetry is not imposed.

It follows from a Schwartz–Christoffel transformation that [2]

$$\frac{1}{U_A D}\int_S U_o(s) n_x \,\mathrm{d}s = 3.34$$

and we may write the non-dimensional frictional force in the ambient flow direction as

$$\frac{F_\mathrm{f}}{\frac{1}{2}\rho U_A^2 D} = \frac{16.744}{KC\sqrt{\beta}}\sin\left(\omega t + \frac{\pi}{4}\right).$$

Table 14 presents the comparison between the numerical and the theoretical non-dimensional frictional force amplitude. The agreement is found to be satisfactory at the lowest Keulegan–Carpenter numbers where the effect of flow separation is restricted to small regions near the corners. The estimated magnitude of the normal viscous force amplitude, given in Table 14, shows that this component is small compared to the frictional force. For $KC \geqslant 0.7$ it was not possible to extract a grid independent solution for $C_{\mathrm{n}\nu,\mathrm{a}}$ using the Richardson extrapolation since this approach predicted a negative amplitude. But it should be noted that the calculated value for $C_{\mathrm{n}\nu,\mathrm{a}}$ decreased as the grid was refined. For instance, at $KC = 1.5$ we obtained $C_{\mathrm{n}\nu,\mathrm{a}} = 0.0529$, 0.0355 and 0.0207, respectively, on the three different grids starting with the coarsest. The numerical estimation on the finest grid can still be considered to be small compared to the skin friction force amplitude. There is a satisfactory agreement between the calculated frictional phase angle α_ν and the theoretical value, which is approximately 0.785, at the lowest KC numbers. The calculated frictional force phase lead relative to the ambient flow velocity increases with KC as shown in Table 14.

The total streamwise force due to the boundary layer may be written in terms of Morison's Eq. (24) as [2]

$$C_{\mathrm{DBL}} = \frac{27.90}{KC\sqrt{\beta}} \quad \text{and} \quad C_{\mathrm{MBL}} = \frac{2.40}{\sqrt{\beta}}.$$

Then from a Schwartz–Christoffel transformation the added mass coefficient, A_{11}, is found to be $1.189\rho D^2$. This contributes $C_{\mathrm{M}o} = 2.787$ to the total mass coefficient, C_M, due to the outer inviscid flow. The effect of vortex shedding in terms of the in-line force coefficients may be written as [2]

$$C_{\mathrm{D}\nu} = 4.159 \quad \text{and} \quad C_{\mathrm{M}\nu} = -0.417KC.$$

The total streamwise force coefficients for a facing square section may then be expressed as

$$C_\mathrm{D} = 4.159 + \frac{1.91}{KC} \quad \text{and} \quad C_\mathrm{M} = 2.951 - 0.417KC$$

when $\beta = 213$.

Fig. 25 compares the calculated mass and drag coefficients with the experimental and theoretical results of Bearman et al. [2] and the numerical results of Herfjord [28]. We note that the theoretical C_D coefficient is in good agreement with our predictions for $KC \leqslant 0.2$. For larger KC numbers the drag coefficients based on our numerical method drops more rapidly than the theoretical curve and predicts a lower drag coefficient. The mass coefficients obtained from our numerical calculations remain nearly constant for $KC \leqslant 1$. There is a

Table 14
Comparison of numerical and theoretical coefficients of frictional force amplitude $C_{\mathrm{f,a}}$, normal viscous force amplitude $C_{\mathrm{n}\nu,\mathrm{a}}$, and frictional force phase lead relative to the ambient flow velocity α_ν

KC	Theory	Present		
	$C_{\mathrm{f,a}}$	$C_{\mathrm{f,a}}$	$C_{\mathrm{n}\nu,\mathrm{a}}$	α_ν
0.1	11.47	11.16	6.1×10^{-2}	0.793
0.2	5.734	5.579	2.9×10^{-2}	0.800
0.5	2.294	2.219	2.6×10^{-3}	0.842
0.7	1.638	1.566	–	0.889
1.0	1.147	1.065	–	0.986
1.2	0.956	0.880	–	1.052
1.5	0.765	0.713	–	1.125

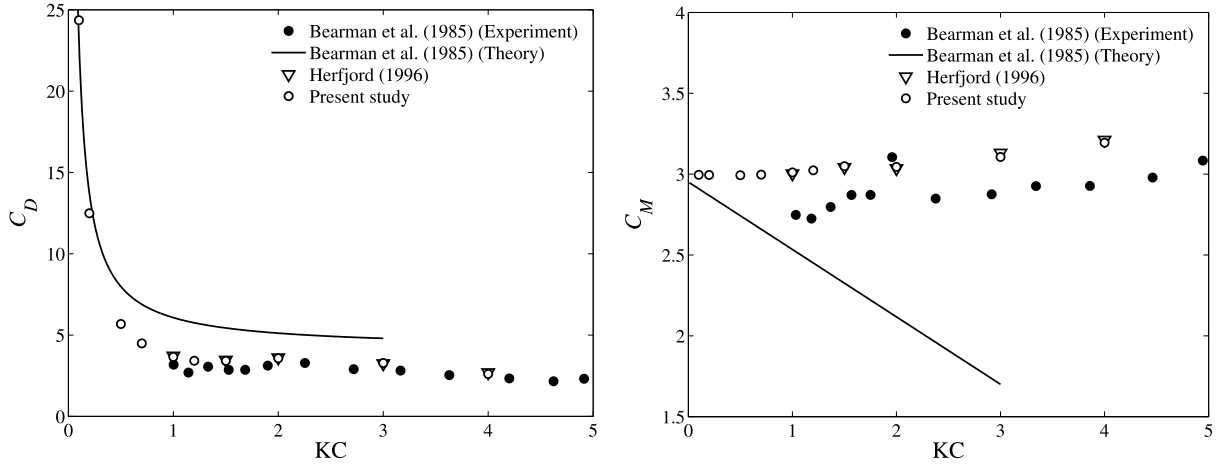

Fig. 25. Drag and mass coefficients for a facing square section in oscillating flow where $\beta = 213$.

small, but growing increase in C_M for larger Keulegan–Carpenter numbers. On the contrary, the theoretical C_M curve has a negative slope predicting much lower values for the mass coefficient. An important error source in the theoretical method is believed to be associated with the predictions of the contribution from flow separation. The present results compare well with the data of Herfjord [28]; however, the computed C_D and C_M coefficients are slightly larger than those obtained from the measurements [2].

For $KC \geqslant 2$ the flow is no longer symmetric and regular, such that the sampled data becomes very sensitive to the time window which they are collected from. For these Keulegan–Carpenter numbers, there is larger uncertainty about the numerical accuracy. Also, there are possibilities of turbulence and other three-dimensional effects in the experiments which may lead to differences to the two-dimensional laminar calculations. As for the circular cylinder, it is not expected that the numerical results should reproduce the experimental data properly. Thus, the numerical results for higher KC numbers are presented only to show that the trends of the calculated two-dimensional force coefficients are similar to the experimental ones.

5.4.3. A chamfered plate in oscillatory flow

In the final example, we consider oscillatory flow around a chamfered plate facing the flow, as illustrated in Fig. 23, which is identical to the one used in the experiment described by Bearman et al. [2]. The computational setup is similar to the ones used in the previous two examples. The Stokes parameter β is equal to 439, and numerical calculations are performed for KC numbers in the range 0.1–4 where D is the height of the plate. We have enforced numerical symmetry for $KC \leqslant 0.5$.

Table 15 summarize the grid dependence study for $KC = 0.5$. The data presented are given for one period sampled from the twentieth oscillation cycle. Three different grid resolutions are considered where the grid cell spacing on the coarsest grid is $\Delta x = \Delta y = 2.5D$ and the number of refinement levels are 8. The number of time steps per period is set equal to 5000 due to numerical stability constraints. We notice that the differences in the obtained force coefficients decrease as the grid is refined. Unfortunately, the mass coefficient does not show a

Table 15
Grid dependence study for harmonically oscillating flow past a chamfered plate for $\beta = 439$ and $KC = 0.5$: oscillation period T, time step Δt, minimum grid resolution near cylinder wall $\Delta x_{\min}$, drag coefficients C_D, and mass coefficient C_M

Domain size	Time step	Grid		Results	
	$\frac{T}{\Delta t}$	Base grid	$\frac{D}{\Delta x_{\min}}$	C_D	C_M
$40D \times 20D$	5000	16×8	102.4	8.48910	1.30029
$40D \times 20D$	5000	32×16	204.8	8.13506	1.30505
$40D \times 20D$	5000	64×32	409.6	8.00830	1.30293

monotone convergence. The flow is nearly singular at the edge of the plate such that monotone convergence is not necessarily possible to obtain, even with further grid refinements. The consequence is that we can not estimate the order of convergence, γ, which we need for the Richardson extrapolation (22) to approximate the numerical error. However, the differences between the force coefficients obtained on the two finest grids are already small such that the numerical error on the finest grid is expected to be small.

A conservative approach to approximate the numerical error is to use a low order convergence rate, for instance $\gamma = 1$. After all, the Richardson extrapolation gives only an approximate estimation of the numerical error and the only purpose is to provide a reasonable guess on the accuracy of the numerical results. Table 16 presents a rough estimation of the relative numerical error based on $\gamma = 1$ for $KC \leqslant 0.5$. We notice that the predicted numerical error is very low for $KC \leqslant 0.2$. It is somewhat larger for KC equal to 0.4 and 0.5, but still acceptable as the streamwise force is dominated by the mass term in Eq. (24) and the error remains low for C_M.

The non-dimensional frictional force in the ambient flow direction may be written as [2]

$$\frac{F_f}{\frac{1}{2}\rho U_A^2 D} = \frac{4.081}{KC\sqrt{\beta}} \sin\left(\omega t + \frac{\pi}{4}\right).$$

The comparison between the numerical and theoretical frictional force amplitude coefficient $C_{f,a}$ together with the calculated $C_{nv,a}$ coefficient and the frictional phase lead α_v are given in Table 17. The agreement between the theoretical and numerical frictional force amplitude is good for $KC \leqslant 0.2$. For larger Keulegan–Carpenter number the theory predicts a much lower value for the frictional force than what is obtained by the present numerical method. The estimated normal viscous force is small compared to the frictional force for all cases. The calculated phase lead is larger than the theoretical value of approximately 0.785. The agreement with theory is fairly acceptable for $KC = 0.1$, but the discrepancy is somewhat larger for the other cases.

The mass coefficient based on potential flow theory for the present chamfered plate is $C_{Mo} = 1.169$. The contribution to the force coefficients from the boundary layer is $C_{MBL} = 0.028$ and $C_{DBL} = 0.325/KC$ for $\beta = 439$. The effect of vortex shedding may be written as $C_{Dv} = 7.761KC^{-1/7}$ and $C_{Mv} = -0.042KC^{6/7}$ such that the total in-line force coefficients for a chamfered plate can be expressed as [2]

$$C_D = 7.761KC^{-1/7} + \frac{0.325}{KC} \quad \text{and} \quad C_M = 1.197 - 0.042KC^{6/7}.$$

As shown in Fig. 26, the numerically calculated C_D coefficient agrees well with the theoretical curve for $KC = 0.1$. The theoretical curve has a steep negative slope at small Keulegan–Carpenter numbers; however,

Table 16
Calculated force coefficients for a chamfered plate in oscillating flow where $\beta = 439$: Drag coefficient C_D and mass coefficient C_M obtained on the finest grid, relative error $\bar{\epsilon}_h$ based on $\gamma = 1$

KC	C_D	$\bar{\epsilon}_h(C_D)$ (%)	C_M	$\bar{\epsilon}_h(C_M)$ (%)
0.1	13.2043	0.31	1.27421	−0.025
0.2	8.25450	−0.21	1.27423	−0.060
0.4	7.61011	−1.43	1.29046	−0.13
0.5	8.00830	−1.58	1.30293	−0.16

Table 17
Comparison of numerical and theoretical coefficients of frictional force amplitude $C_{f,a}$, normal viscous force amplitude $C_{nv,a}$, and frictional force phase lead relative to ambient flow velocity α_v

KC	Theory	Present		
	$C_{f,a}$	$C_{f,a}$	$C_{nv,a}$	α_v
0.1	1.948	1.910	4.4×10^{-2}	0.857
0.2	0.974	0.987	2.2×10^{-2}	0.934
0.4	0.487	0.577	1.1×10^{-2}	1.027
0.5	0.390	0.487	8.0×10^{-3}	0.984

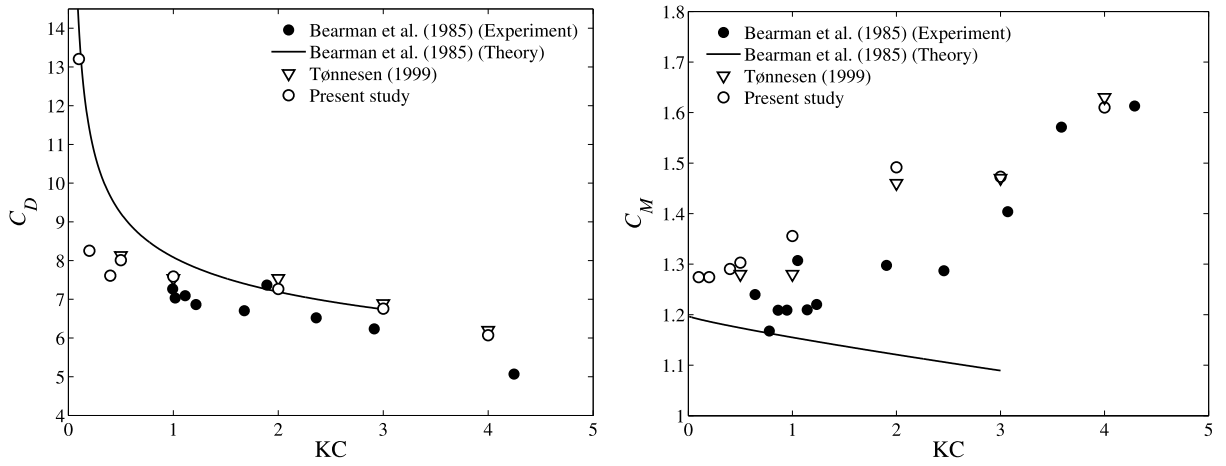

Fig. 26. Drag and mass coefficients for a chamfered plate in oscillating flow where $\beta = 439$.

the numerically calculated drag coefficient drops more rapidly and there is a large discrepancy between the theory and the present method for $0.1 < KC < 1.0$. At larger KC numbers the theoretical curve fits closely to the C_D coefficients obtained by the numerical method. The calculated drag coefficients are close to the numerical results obtained by [72], but they are somewhat larger than the experimental data presented by [2]. Fig. 26 shows that the theory predicts a much lower C_M coefficient than what is obtained by experimental measurements and numerical methods. The present numerical method gives a nearly constant mass coefficient for the lowest Keulegan–Carpenter numbers. Thereafter, it grows for larger KC numbers, except for a small adjustment in the trend at $KC \approx 3$. The mass coefficients based on the present numerical method agree well with [72], except for $KC = 1$. Both numerical methods tend to over predict the measured C_M coefficients, particularly at the intermediate KC numbers. It should be pointed out that the flow is asymmetric and irregular for $KC \geqslant 1.0$, meaning that the force coefficients are very sensitive to the choice of sampling period and a long simulation time is required. A grid dependence study is therefore not affordable for larger KC numbers, resulting in an increased uncertainty about the numerical accuracy. For these Keulegan–Carpenter numbers, it is likely that the vortices shed from the edge of the plate rapidly becomes three-dimensional due to spanwise instabilities and, eventually, become turbulent. As for the two previous examples, the two-dimensional laminar calculations will in that case not necessarily capture all the correct details of the flow from the experiment, but we may notice that it follows a nearly similar trend.

6. Summary and conclusion

An immersed boundary method for solving the incompressible Navier–Stokes equation in irregular domains has been presented. The solid boundary has been treated by a local one-dimensional ghost cell approach. This method smoothly extends the solution across the boundary along the same direction as the discretization it will be used for. The local feature of the present method allows for highly irregular boundaries (e.g. sharp corners) to be treated accurately. A local, block structured grid refinement technique has been adopted in order to enhance the computational efficiency. Numerical experiments have shown that the spatial accuracy of the numerical method is second order.

We have applied the present technique to a series of test problems involving steady and unsteady flow past stationary objects. This includes uniform flow past a circular cylinder, impulsively started flow past a circular cylinder and a flat plate, and planar oscillating flow past a circular cylinder, a facing square and a chamfered plate. For the uniform flow past a circular cylinder, we showed that our method is capable of detecting the onset of flow instability. Calculated force coefficients and Strouhal numbers are found to be well within the range of data reported by others. In the case of impulsively started flow, we demonstrated that our approach is fully capable of predicting the time evolution of the wake behind a stationary object. The local solutions of the flow compared satisfactorily with both experimental measurements and other numerical methods.

For a circular cylinder in oscillating flow we obtained good agreement with attached flow theory at low Keulegan–Carpenter numbers. For larger KC numbers the theory is no longer valid as separation and vortex shedding has become more important. The calculated drag and mass coefficients showed good agreement with experimental results for small KC numbers where the flow is attached, laminar and strictly two-dimensional. Due to three-dimensional effects there was a small difference between numerical and experimental results for larger KC numbers, but the trend was otherwise nearly similar.

In the case of a sharp-edged cylinder, such as a square and a plate, the flow will separate even at small KC numbers. However, numerical simulations compare satisfactorily with attached flow theory at the lowest KC numbers where the effect of flow separation is concentrated near the edges. The calculated drag and mass coefficients are somewhat larger than those obtained from experiments. In the range of KC numbers where experimental data are available it is believed that three-dimensional effects are present. In that case, it is not expected that the present two-dimensional laminar approach should reproduce the measurements properly, but the trends seem to be similar and our results are comparable with other numerical methods.

In the present work we have only applied our method to two-dimensional flow problems, but we believe that an extension to three-dimensional problems is rather straight forward. Following the concept described in this work, the immersed boundary can be treated by one-dimensional extrapolation in the third dimension as well.

Acknowledgments

This work was sponsored by the Centre of Ships and Ocean Structures, Norwegian Centre of Excellence at Norwegian University of Science and Technology (NTNU), through The Research Council of Norway (NFR). It has also received support from NTNU and NFR (Programme for Supercomputing) through a grant of computing time.

References

[1] E. Balaras, Modeling complex boundaries using an external force field on fixed Cartesian grids in large-eddy simulations, Comput. Fluids 33 (3) (2004) 375–404.
[2] P.W. Bearman, M.J. Downie, J.M.R. Graham, E.D. Obasaju, Forces on cylinders in viscous oscillatory flow at low Keulegan–Carpenter numbers, J. Fluid Mech. 154 (1985) 337–356.
[3] M. Berger, I. Rigoutsos, An algorithm for point clustering and grid generation, IEEE Trans. Syst. Man Cybernet. 21 (5) (1991) 1278–1286.
[4] P.A. Berthelsen, A decomposed immersed interface method for variable coefficient elliptic equations with non-smooth and discontinuous solutions, J. Comput. Phys. 197 (1) (2004) 364–386.
[5] R. Bouard, M. Coutanceau, The early stage of development of the wake behind an impulsively started cylinder for $40 < Re < 10^4$, J. Fluid Mech. 101 (3) (1980) 583–607.
[6] M. Bozkurttas, H. Dong, V. Seshadri, R. Mittal, F. Najjar, Towards numerical simulation of flapping foils on fixed Cartesian grids, in: AIAA 43rd Aerospace Sciences Meeting and Exhibit, Reno, Nevada, USA, 10–13th January, 2005, AIAA 2005-0079.
[7] M. Bozkurttas, H. Dong, R. Mittal, P. Madden, G.V. Lauder, Hydrodynamic performance of deformable fish fins and flapping foils, in: AIAA 44th Aerospace Sciences Meeting and Exhibit, Reno, Nevada, USA, 9–12th January, 2006, AIAA 2006-1392.
[8] M. Braza, P. Chassaing, H. Ha Minh, Numerical study and physical analysis of the pressure and velocity fields in the near wake of a circular cylinder, J. Fluid Mech. 165 (1986) 79–130.
[9] D. Calhoun, A Cartesian grid method for solving the two-dimensional streamfunction-vorticity equations in irregular regions, J. Comput. Phys. 176 (2) (2002) 231–275.
[10] A.J. Chorin, Numerical solution of the Navier–Stokes equations, Math. Comput. 22 (1968) 742–762.
[11] M. Coutanceau, R. Bouard, Experimental determination of the main features of the viscous flow in the wake of a circular cylinder in uniform translation. Part 1. Steady flow, J. Fluid Mech. 79 (2) (1977) 231–256.
[12] S.C.R. Dennis, G.-Z. Chang, Numerical solutions for steady flow past a circular cylinder at Reynolds numbers up to 100, J. Fluid Mech. 42 (3) (1970) 471–489.
[13] D. DeZeeuw, K.G. Powell, An adaptively refined Cartesian mesh solver for the Euler equations, J. Comput. Phys. 104 (1) (1993) 56–68.
[14] E.A. Fadlun, R. Verzicco, P. Orlandi, J. Mohd-Yusof, Combined immersed-boundary finite-difference methods for three-dimensional complex flow simulation, J. Comput. Phys. 161 (1) (2000) 35–60.
[15] O.M. Faltinsen, Sea Loads on Ships and Offshore Structures, Cambridge University Press, Cambridge, England, 1990.
[16] J.H. Ferziger, M. Perić, Computational Methods for Fluid Dynamics, third ed., Springer-Verlag, Berlin, Germany, 2002.
[17] H. Forrer, R. Jeltsch, A higher-order boundary treatment for Cartesian-grid methods, J. Comput. Phys. 140 (2) (1998) 259–277.

[18] R. Ghias, R. Mittal, T.S. Lund, A non-body conformal grid method for simulation of compressible flows with complex immersed boundaries, in: 42nd AIAA Aerospace Sciences Meeting and Exhibit, Reno, Nevada, USA, 5–8 January, 2004.
[19] F. Gibou, R.P. Fedkiw, L.-T. Cheng, M. Kang, A second-order-accurate symmetric discretization of the Poisson equation on irregular domains, J. Comput. Phys. 176 (1) (2002) 205–227.
[20] A. Gilmanov, F. Sotiropoulos, E. Balaras, A general reconstruction algorithm for simulating flows with complex 3D immersed boundaries on Cartesian grids, J. Comput. Phys. 191 (2) (2003) 660–669.
[21] A. Gilmanov, F. Sotiropoulos, A hybrid Cartesian/immersed boundary method for simulating flows with 3D, geometrically complex, moving bodies, J. Comput. Phys. 207 (2) (2005) 457–492.
[22] D. Goldstein, R. Handler, L. Sirovich, Modeling a no-slip flow boundary with an external force field, J. Comput. Phys. 105 (2) (1993) 354–366.
[23] J.M.R. Graham, The forces on sharp-edged cylinders in oscillatory flow at low Keulegan–Carpenter numbers, J. Fluid Mech. 97 (1980) 331–346.
[24] A.S. Grove, F.H. Shair, E.E. Petersen, A. Acrivos, An experimental investigation of the steady separated flow past a circular cylinder, J. Fluid Mech. 19 (1964) 60–80.
[25] X. He, G. Doolen, Lattice Boltzmann method on curvilinear coordinate system: flow around a circular cylinder, J. Comput. Phys. 134 (2) (1997) 306–315.
[26] R.D. Henderson, Details of the drag curve near the onset of vortex shedding, Phys. Fluids 7 (9) (1995) 2102–2104.
[27] R.D. Henderson, Nonlinear dynamics and pattern formation in turbulent wake transition, J. Fluid Mech. 352 (1997) 65–112.
[28] K. Herfjord, A study of two-dimensional separated flow by a combination of the finite element method and Navier–Stokes equations, Dr. Ing.-Thesis, Norwegian Institute of Technology, Department of Marine Hydrodynamics, Trondheim, Norway, 1996.
[29] H. Honji, Streaked flow around an oscillating circular cylinder, J. Fluid Mech. 107 (1981) 509–520.
[30] G.-S. Jiang, D. Peng, Weighted ENO schemes for Hamilton–Jacobi equations, SIAM J. Sci. Comput. 21 (6) (2000) 2126–2143.
[31] G.-S. Jiang, C.-W. Shu, Efficient implementation of weighted ENO schemes, J. Comput. Phys. 126 (1) (1996) 202–228.
[32] M. Kang, R.P. Fedkiw, X.-D. Liu, A boundary condition capturing method for multiphase incompressible flow, J. Sci. Comput. 15 (3) (2000) 323–360.
[33] G.H. Keulegan, L.H. Carpenter, Forces on cylinders and plates in an oscillating fluid, J. Res. Natl. Bur. Standards 60 (5) (1958) 423–440.
[34] J. Kim, D. Kim, H. Choi, An immersed-boundary finite-volume method for simulations of flow in complex geometries, J. Comput. Phys. 171 (1) (2001) 132–150.
[35] M.P. Kirkpatric, S.W. Armfield, J.H. Kent, A representation of curved boundaries for the solution of the Navier–Stokes equations on a staggered three-dimensional Cartesian grid, J. Comput. Phys. 184 (1) (2003) 1–36.
[36] P. Koumoutsakos, A. Leonard, High-resolution simulations of the flow around an impulsively started cylinder using vortex methods, J. Fluid Mech. 296 (1995) 1–38.
[37] P. Koumoutsakos, D. Shiels, Simulations of the viscous flow normal to an impulsively started and uniformly accelerated flat plate, J. Fluid Mech. 328 (1996) 177–227.
[38] M.-C. Lai, C.S. Peskin, An immersed boundary method with formal second-order accuracy and reduced numerical viscosity, J. Comput. Phys. 160 (2) (2000) 705–719.
[39] D.V. Le, B.C. Khoo, J. Peraire, An immersed interface method for viscous incompressible flows involving rigid and flexible boundaries, J. Comput. Phys. 220 (1) (2006) 109–138.
[40] Y. Lecointe, J. Piquet, On the use of several compact methods for the study of unsteady incompressible viscous flow round a circular cylinder, Comput. Fluids 12 (4) (1984) 255–280.
[41] R.J. Leveque, Z. Li, The immersed interface method for elliptic equations with discontinuous coefficients and singular sources, SIAM J. Numer. Anal. 31 (4) (1994) 1019–1044.
[42] R.J. Leveque, Z. Li, Immersed interface method for Stokes flow with elastic boundaries or surface tension, SIAM J. Sci. Comput. 18 (3) (1997) 709–735.
[43] Z. Li, M.-C. Lai, The immersed interface method for the Navier–Stokes equations with singular forces, J. Comput. Phys. 171 (2) (2001) 822–842.
[44] Z. Li, C. Wang, A fast finite difference method for solving Navier–Stokes equations on irregular domains, Commun. Math. Sci. 1 (1) (2003) 180–196.
[45] M. N Linnick, H.F. Fasel, A high-order immersed interface method for simulating unsteady compressible flows on irregular domains, J. Comput. Phys. 204 (1) (2005) 157–192.
[46] H. Liu, S. Krishnan, S. Marella, H.S. Udaykumar, Sharp interface Cartesian grid method II: a technique for simulating droplet interactions with surfaces of arbitrary shape, J. Comput. Phys. 210 (1) (2005) 32–54.
[47] X.-D. Liu, R.P. Fedkiw, M. Kang, A boundary condition capturing method for Poisson's equation on irregular domains, J. Comput. Phys. 160 (1) (2000) 151–178.
[48] S. Majumdar, G. Iaccarino, P. Durbin, RANS solvers with adaptive structured boundary non-conforming grids, Annu. Res. Briefs, Cent. Turbul. Res. (2001) 353–366.
[49] S. Marella, S. Krishnan, H. Liu, H.S. Udaykumar, Sharp interface Cartesian grid method I: an easily implemented technique for 3D moving boundary computations, J. Comput. Phys. 210 (1) (2005) 1–31.
[50] D.F. Martin, K. Cartwright, Solving Poisson's equation using adaptive mesh refinement, Technical Report UCB/ERI M96/66, U.C. Berkeley, California, USA, 1996. <http://seesar.lbl.gov/ANAG/publication.html>.
[51] R. Mittal, G. Iaccarino, Immersed boundary methods, Annu. Rev. Fluid Mech. 37 (2005) 239–261.

[52] X.D. Niu, Y.T. Chew, C. Shu, Simulation of flows around an impulsively started circular cylinder by Taylor series expansion- and least square-based lattice Boltzmann method, J. Comput. Phys. 188 (1) (2003) 176–193.
[53] D. Pan, An immersed boundary method for incompressible flows using volume of body function, Int. J. Numer. Methods Fluids 50 (6) (2006) 733–750.
[54] J. Park, K. Kwon, H. Choi, Numerical solutions of flow past a circular cylinder at Reynolds numbers up to 160, KSME Int. J. 12 (1998) 1200–1205.
[55] C.S. Peskin, Flow patterns around heart valves: a numerical method, J. Comput. Phys. 10 (2) (1972) 252–271.
[56] C.S. Peskin, Numerical analysis of blood flow in the heart, J. Comput. Phys. 25 (3) (1977) 220–252.
[57] J.J. Quirk, An alternative to unstructured grids for computing gas dynamic flows around arbitrarily complex two-dimensional bodies, Comput. Fluids 23 (1) (1994) 125–142.
[58] D. Russel, Z.J. Wang, A Cartesian grid method for modeling multiple moving objects in 2D incompressible viscous flow, J. Comput. Phys. 191 (1) (2003) 177–205.
[59] Y. Saad, SPARSKIT: a basic tool kit for sparse matrix computations, ver. 2, Technical Report, Research Institute for Advanced Computer Science, NASA Ames Research Center, Moffet Field, California, USA, 1994. <http://www-users.cs.umn.edu/saad/software/SPARSKIT/sparskit.html>.
[60] Y. Saad, Iterative Methods for Sparse Linear Systems, second ed., Society for Industrial and Applied Mathematics, Philadelphia, Pennsylvania, USA, 2003.
[61] E.M. Saiki, S. Biringen, Numerical simulation of a cylinder in uniform flow: application of a virtual boundary method, J. Comput. Phys. 123 (2) (1996) 450–465.
[62] T. Sarpkaya, Force on a circular cylinder in viscous oscillatory flow at low Keulegan–Carpenter numbers, J. Fluid Mech. 165 (1986) 61–71.
[63] S.-W. Su, M.-C. Lai, C.-A. Lin, An immersed boundary technique for simulating complex flows with rigid boundary, Comput. Fluids 36 (2) (2007) 313–324.
[64] B.M. Sumer, J. Fredsøe, in: Hydrodynamics Around Cylindrical Structures, Advanced series on Ocean Engineering, vol. 12, World Scientific Publishing, Singapore, 1997.
[65] Ta Phuoc Loc, Numerical analysis of unsteady secondary vortices generated by an impulsively started circular cylinder, J. Fluid Mech. 100 (1) (1980) 111–128.
[66] S. Tanji, H. Honji, Unsteady flow past a flat plate normal to the direction of motion, J. Phys. Soc. Jpn. 30 (1) (1971) 262–272.
[67] F. Tremblay, Direct and large-eddy simulation of flow around a circular cylinder at subcritical Reynolds numbers, Dr.Ing. Dissertation, Technischen Universität München, Fachgebiet Strömungsmechanik, Germany, 2001. <http://www-waterloo.ansys.com/European_Projects/alessia/papers/D5.17_6_Thesis_Tremblay.pdf>.
[68] F. Tremblay, R. Friedrich, An algorithm to treat flows bounded by arbitrarily shaped surfaces with Cartesian meshes, in: Proceedings of AGSTAB Conference, University of Stuttgart, Germany, 15–17th November, 2000.
[69] D.J. Tritton, Experiments on the flow past a circular cylinder at low Reynolds numbers, J. Fluid Mech. 6 (1959) 547–567.
[70] Y.-H. Tseng, J.H. Ferziger, A ghost-cell immersed boundary method for flow in complex geometry, J. Comput. Phys. 192 (2) (2003) 593–623.
[71] Y.-H. Tseng, J.H. Ferziger, Large-eddy simulation of turbulent wavy boundary flow – illustration of vortex dynamics, J. Turbulence 5 (2004).
[72] R. Tønnessen, A finite element method applied to unsteady viscous flow around 2D blunt bodies with sharp corners, Dr.Ing.-Thesis, Norwegian University of Science and Technology, Department of Marine Hydrodynamics, Trondheim, Norway, 1999.
[73] H.S. Udaykumar, W. Shyy, M.M. Rao, ELAFINT: a mixed Eulerian–Lagrangian method for fluid flows with complex and moving boundaries, Int. J. Numer. Methods Fluids 22 (8) (1996) 691–712.
[74] H.S. Udaykumar, R. Mittal, W. Shyy, Computation of solid–liquid phase fronts in the sharp interface limit on fixed grids, J. Comput. Phys. 153 (2) (1999) 535–574.
[75] A. Varges, R. Mittal, Aerodynamic performance of biological airfoils, in: 2nd Flow Control Conference, Portland, Oregon, USA, 28th June–1st July, 2004, AIAA 2004-2319.
[76] C.-Y. Wang, On high-frequency oscillatory viscous flows, J. Fluid Mech. 32 (1968) 55–68.
[77] A. Wiegmann, K.P. Bube, The explicit-jump immersed interface method: finite difference methods for PDEs with piecewise smooth solutions, SIAM J. Numer. Anal. 37 (3) (2000) 827–862.
[78] C.H.K. Williamson, Oblique and parallel modes of vortex shedding in the wake of a circular cylinder at low Reynolds numbers, J. Fluid Mech. 206 (1989) 579–627.
[79] C.H.K. Williamson, Three-dimensional wake transition, J. Fluid Mech. 328 (1996) 345–407.
[80] F.M. White, Viscous Fluid Flow, second ed. (Int. ed.)., McGraw-Hill, Singapore, 1991.
[81] S. Xu, Z.J. Wang, An immersed interface method for simulating the interaction of a fluid with moving boundaries, J. Comput. Phys. 216 (2) (2006) 454–493.
[82] J. Yang, E. Balares, An embedded-boundary formulation for large-eddy simulation of turbulent flows interacting with moving boundaries, J. Comput. Phys. 215 (1) (2006) 12–40.
[83] G. Yang, D.M. Causon, D.M. Ingram, Cartesian cut-cell method for axisymmetric separating body flows, AIAA J. 37 (8) (1999) 905–911.
[84] Y. Yang, H.S. Udaykumar, Sharp interface Cartesian grid method III: solidification of pure materials and binary solutions, J. Comput. Phys. 210 (1) (2005) 54–74.

[85] T. Ye, R. Mittal, H.S. Udaykumar, W. Shyy, An accurate Cartesian grid method for viscous incompressible flows with complex immersed boundaries, J. Comput. Phys. 156 (2) (1999) 209–240.
[86] J.-F. Zou, A.-L. Ren, J. Deng, Study on flow past two spheres in tandem arrangement using a local mesh refinement virtual boundary method, Int. J. Numer. Meth. Fluids 49 (5) (2005) 465–488.
[87] Y.C. Zhou, S. Zhao, M. Feig, G.W. Wei, High order matched interface and boundary method for elliptic equations with discontinuous coefficients and singular sources, J. Comput. Phys. 213 (1) (2006) 1–30.